

**ANALYSIS OF THE EFFECTS OF VEIN ARRANGEMENTS ON
INSECT WING STRUCTURE
WITH FINITE ELEMENT METHOD**

By

Yijun Wang

A thesis submitted to the

Graduate School-New Brunswick

Rutgers, The State University of New Jersey

In partial fulfillment of the requirements

For the degree of

Master of Science

Graduate Program in Mechanical and Aerospace Engineering

Written under the direction of

Dr. Mitsunori Denda

And approved by

New Brunswick, New Jersey

May, 2016

ABSTRACT OF THE THESIS

Analysis of Effects of Vein Arrangements on Insect Wing Structure with Finite Element Method

By YIJUN WANG

Thesis Director:

DR. Mitsunori Denda

Nowadays, the demand for Micro Aerial Vehicles (MAVs) is growing rapidly in both commercial and military use. Due to the excellent flapping flight capability, insects now serve as a main source of biological inspiration for the researches of future micro air vehicles. As the most important organ of flight for insects, insect wing, especially its deformation partially controlled by the vein arrangements, is now becoming a key factor for the research and the design of insect-like MAVs. The purpose of this research is to analyze the effect of the two different kinds of veins and their arrangements on the insect wing structure with Finite Element Method. A simplified wing modelling meshed with the Stiffened Shell Elements is tested under different vein arrangements. The correlated natural frequencies and modeshapes are achieved and analyzed for each case. Through the analysis, we can eventually conclude the effects of longitudinal veins, cross veins and their combined arrangements on the wing structure, respectively.

Acknowledgements

This thesis has been a very rewarding endeavor for me. I really enjoyed the whole research process.

I am very thankful to my advisor Professor Mitsunori Denda for being such a helpful and supportive mentor. When I first started doing this research, I knew almost nothing about the Finite Element Method. With the help of my advisor, I can finally manage to catch up everything I need to know about the structure analysis. His enthusiasm in academics constantly encouraged me to keep overcoming the difficulties and never give up trying. This thesis wouldn't have been possible without his help and guidance.

I would also like to thank the faculty of MAE department and the Rutgers University for providing me great education in the past few years and allowing me to become a better engineer.

I am grateful towards my family and friends for supporting me during the research.

Table of Contents

Abstract of the thesis	ii
Acknowledgements	iii
1. Introduction	1
1.1 The background and purpose of the research	1
1.2 The method of the research.	2
2. Finite Element Method.	4
2.1 Introduction to Faceted Stiffened Shell with Allman Membrane Triangular Element	4
2.2 Components of the Stiffened Shell Element	4
2.2.1 3-D Euler Bernoulli Beam Element	4
2.2.1.1 Rod Element	5
2.2.1.2 2-D Euler Bernoulli Beam Element	8
2.2.1.3 Torsional Behavior.	15
2.2.2 Thin (Kirchhoff) Plate Bending using BCIZ Triangular Element.	16
2.3.3 Allman Membrane Triangular Element	21
2.3 Transformation and Assembly.	26
2.3.1 Assembly of 3-D Euler-Bernoulli Beam Element	26
2.3.2 Transform and Assembly of TriFrame Element.	26
2.3.3 Assembly of Allman Shell Element with drilling degree of freedom.	27
2.3.4 Transform in to Global Coordination.	27
2.3.5 Assembly of Allman Stiffened Shell Element.	27
2.3.6 The Matlab Code.	28

3. Numerical Examples	29
3.1 Finite Element Modelling.....	29
3.2 Experimental Cases.....	30
3.2.1 Case Set 1: Longitudinal Vein Arrangements.....	31
3.2.2 Case Set 2: Cross Vein Arrangements.....	32
3.2.3 Case Set 3: Combined Veins Arrangements.....	33
3.3 Numerical Performance.....	33
3.3.1 The Reference Case.....	34
3.3.2 Effects of the Longitudinal Veins Arrangements.....	36
3.3.2.1 Effects on the Natural Frequencies.....	36
3.3.2.2 Effects on the Modeshapes.....	38
3.3.3 Effects of the Cross Veins Arrangements.....	42
3.3.3.1 Effects on the Natural Frequencies.....	42
3.3.3.2 Effects on the Modeshapes.....	43
3.3.4 Effects of the Combined Veins Arrangements.....	49
3.3.4.1 Effects on the Natural Frequencies.....	49
3.3.4.2 Effects on the Modeshapes.....	50
4. Conclusions and Future Work	55
4.1 Conclusions.....	55
4.2 Future Work.....	56
Reference	57
Appendices	58

Chapter One

Introduction

1.1 The background and purpose of the research

In the past few years, the demand for Micro Air Vehicles (MAVs) has been growing at a rapid pace. Its advantages in versatility, maneuverability, cost-efficient and counter-observation ability makes it increasingly popular in both civil and military use. Insects now serve as a main source of biological inspiration for the researches of future micro air vehicles due to their excellent flapping flight capability. Especially for the unmanned intelligence, surveillance and reconnaissance purposes, insect's ability to hover in flapping flight and its feature of micro geometry size make it an incomparable research target.

As the organ of flight for insects, insect wings are extraordinary examples of small-scale biological engineering: small, flexible aerofoils with no parallels in technology [5]. By studying and understanding the functions of the wing structures, one may get closer to reproduce the flight features of insects on MAVs. Most of the wing consist of membrane supported by veins [7]. Here, the veins are cuticular tubes containing hemolymph and often tracheae and nerves. There are two kinds of veins. One is main or longitudinal vein, which radiates from the base, often branching distally, and the other one is cross-vein, which links the longitudinal veins [7].

Other than supporting the membrane, the veins on the wing structure also play a major role in the flight of insects. In flapping flight, insect wings not only change their direction movement and their angle of attack relative to the airflow, they undergo deformation, which may actually be necessary for the generation of sufficient aerodynamic force [7]. The deformation of the wings is partially controlled by the active muscular forces. However, the forces cannot entirely control the wing shape. They can only

interact dynamically with the aerodynamic and inertial forces that the wings experience and with the wing's own elasticity. The instantaneous results of these interactions are essentially determined by the architecture of the wing itself [7].

In this research, we mainly focus on one of the most important features of the wing's architecture: the distribution of the veins. Through analyzing the effect of different distributions of the veins on the wing's deformation, we will have a clearer idea of how different kinds of veins and their combinations will affect the wing's performance during the flight and we will be one step closer to design a much more efficient wing structure with optimized vein distribution for the future insect-like Micro Air Vehicles.

1.2 The method of the research

The Finite Element Method is among the most commonly used structural dynamic analysis method when it comes to the researches on the insect wing structure. In most cases, a certain species of insect is chosen as the research object [1,2,4]. During the researches, the characteristics of wing structures are found through various experiments and correlated Finite Element Modelling [1-4,6]. It seems to be reasonable and guaranteed to apply such method to the current research. However, such technique fails to fulfill the requirements of the research.

The purpose of the research is not to replicate the performance of specific wing structures, but to analyze the effect of veins on the wing structure in a general setting. Thus we use a simplified wing model and set up different test cases, each corresponding to a different vein distribution. Then the wing model is meshed with a special customized shell element, that is, the Faceted Stiffened Shell with Allman Membrane Triangular Element. The stiffness matrix and the mass matrix of the selected element is derived to form the linear eigenvalue problem equation of structural dynamics. A matlab program is developed to solve the problem and get the natural frequencies, as well as the related modeshapes for

each test case. By aforementioned technique, we can eventually find out how different kinds of veins and their distributions affect the wing structure.

Chapter Two

Finite Element Method

2.1 Introduction to Faceted Stiffened Shell with Allman Membrane Triangular Element

The Faceted Stiffened Shell with Allman Membrane Triangular Element is a triangular element that consists of the Kirchhoff Plate Bending Element, Allman Membrane Element and 3-D Euler Bernoulli Beam Element. Here, the 3-D Euler Bernoulli Beam Elements are used to stiffen the edges of the triangular shell element, of which the purpose is to reproduce the function of veins in the following dynamic structure analysis. The stiffened shell element has six degrees of freedom, which ensures it to display the structure deformation correctly.

2.2 Components of the Stiffened Shell Element

2.2.1 3-D Euler Bernoulli Beam Element

The 3-D Euler Bernoulli Beam Element is an extension of 2-D Bernoulli model. Therefore, the 3-D Element should be developed within the structure already defined for the 2-D beams and more generally for all structural mechanics elements [8]. More specifically, it is developed based on the 2-D Euler Bernoulli Beam Element, Rod Element and Torsion Element in the same defined structure. All the three elements follow Bernoulli's law. It corresponds to the relation expressed as: *Planar cross sections which are perpendicular to the axis will be conserved in deformed configuration*. Detailed derivation of each element is discussed in the following sections.

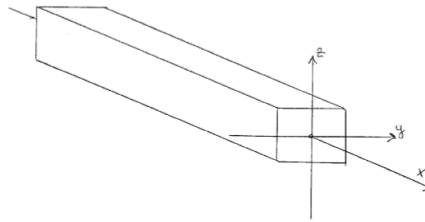


Fig 2.0 System of coordinates considered in this section [8]

2.2.1.1 Rod Element

The Rod Element represents the axial behavior of the 3-D beam element, of which the statement is shown in the figure below. As we can see in the figure, the cross section of the rod has a constant area A . Here, N denotes the normal stress and $u(x)$ is the displacement field. $q(x)$ is the given distributed load along the rod's surface.

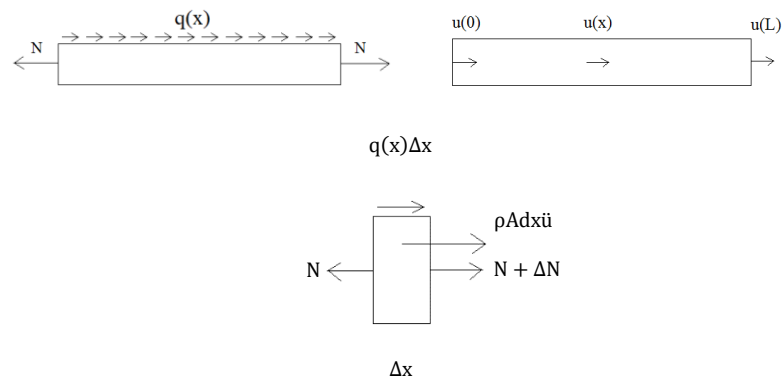


Fig 2.1 Axial Behavior

Kinematic relation, which is derived from the Bernoulli's law, and Stress-Strain relation are shown below:

$$\epsilon_{xx} = \frac{\partial u}{\partial x} \quad \sigma_{xx} = E\epsilon_{xx} \tag{1}$$

with ϵ_{xx} the axial strain.

Equation of motion is given by

$$N + \Delta N - N + q(x)\Delta x = \rho A dx \ddot{u}$$

$$\frac{dN}{dx} + q(x) = \rho A \ddot{u} \quad (2a)$$

Where

$$N = \int_A \sigma_{xx} dA = \int_A E \frac{du}{dx} dA = EA \frac{du}{dx} = EA \varepsilon_{xx} \quad (2b)$$

After getting the equations above, we can now apply the P.V.W, that is, the principle of virtual work, to get the finite element formula of the element. The equilibrium field is

$$\frac{dN^*}{dx} + q^*(x) = \rho A \ddot{u}^*$$

And the compatible field is

$$\hat{\varepsilon}_{xx} = \frac{d\hat{u}}{dx}$$

Then we can get the integral equation:

$$\begin{aligned} \int_0^L N^* \hat{\varepsilon}_{xx} dx &= \int_0^L N^* \frac{d\hat{u}}{dx} dx = [N^* \hat{u}]_0^L - \int_0^L \frac{dN^*}{dx} \hat{u} dx \\ &= [N^* \hat{u}]_0^L + \int_0^L q^*(x) \hat{u} dx - \int_0^L \rho A \ddot{u}^* \hat{u} dx \end{aligned} \quad (3)$$

The generalized displacements at end points are:

$$\Delta_1 = u(0), \quad \Delta_2 = u(L) \quad (4)$$

And the generalized forces are:

$$Q_1 = -N(0), \quad Q_2 = N(L) \quad (5)$$

Therefore, equation (3) becomes

$$\int N^* \hat{\epsilon}_{xx} dx = \sum_{k=1}^2 Q_k^* \hat{\Delta}_k + \int_0^L q^* \hat{u} dx - \int_0^L \rho A \ddot{u}^* \hat{u} dx \quad (6)$$

The selected interpolation polynomial for u

$$u = a_0 + a_1 x$$

that satisfies (4) is given by

$$u(x) = \sum_{k=1}^2 \Delta_k \phi_k \quad (7)$$

Where

$$\phi_1(x) = 1 - \frac{x}{L}, \quad \phi_2(x) = \frac{x}{L}$$

With the equations above, we can now start deriving the FEM formulation by selecting

$$u^* = \sum_{j=1}^2 \Delta_j \phi_j \quad \text{and} \quad \hat{u} = \phi_i$$

in

$$\int_0^L AE \left(\sum_{j=1}^2 \phi_j' \Delta_j \right) \hat{\phi}_i' dx = Q_i + \int_0^L q^* \phi_i dx - \int_0^L \rho A \left(\sum_{j=1}^2 \phi_j \ddot{\Delta}_j \right) \phi_i dx$$

And then we have:

$$\sum_{j=1}^2 AE \left(\int_0^L \phi_j' \phi_i' dx \right) \Delta_j = Q_i + \int_0^L q^* \phi_i dx - \sum_{j=1}^2 \rho A \left(\int_0^L \phi_j \phi_i dx \right) \ddot{\Delta}_j$$

It can also be shown in the form:

$$\sum_{j=1}^2 K_{ji} \Delta_j + \sum_{j=1}^2 M_{ji} \ddot{\Delta}_j = F_i \quad (8)$$

where

$$K_{ji} = AE \int_0^L \phi_j' \phi_i' dx$$

$$M_{ji} = \rho A \int_0^L \phi_j \phi_i dx$$

Here, K and M are the stiffness matrix and the mass matrix of the rod element, respectively. The matrix form of K and M are shown below:

$$K = \frac{AE}{L} \begin{bmatrix} 1 & -1 \\ -1 & 1 \end{bmatrix} \quad M = \frac{\rho AL}{6} \begin{bmatrix} 2 & 1 \\ 1 & 2 \end{bmatrix} \quad (9)$$

2.2.1.2 2-D Euler Bernoulli Beam Element

The Euler Bernoulli Beam Element and the Timoshenko Beam Element are the two most common elements used in the Finite Element Analysis when it comes to the beam or frame problems. They both represent the planar flexural behavior of a 3-D beam element. In this case, the Euler Bernoulli Beam Element has been chosen since the length-width ratio of the veins on insect wing structure is much larger than 10:1 and the rotation of the cross-section plane is not necessarily to be taken into consideration. The statement of 2-D beam element is shown in the Fig 2.2.

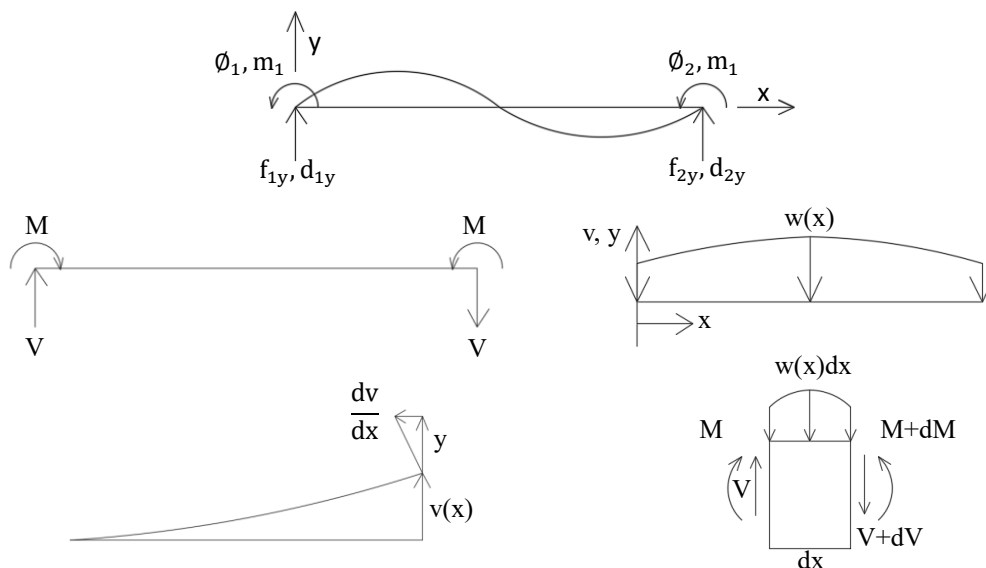


Fig 2.2 Planar Flexural Behavior

As we can see in the figure above, M denotes the bending moment and V denotes the shear force acted on the element. $w(x)$ is the distributed load on the element and $v(x)$ is the displacement in y -direction.

To get the stiffness matrix and the mass matrix of Euler Beam Element, we need to analyze the element

under static condition in the first place, by which mean we can easily achieve the stiffness matrix.

Let's start from the shear force-bending moment-deflection relations. First, we have:

1) Force equilibrium equation

$$-w dx - dV = 0$$

2) Moment equilibrium equation

$$-V dx + dM = 0$$

Rearrange the two equations and we have the following relations:

$$w = -\frac{dV}{dx} \quad V = \frac{dM}{dx}$$

The axial strain and stress are:

$$u = -y \frac{dv}{dx}$$

$$\varepsilon_x = -y \frac{d^2v}{dx^2}$$

$$\sigma_x = E \varepsilon_x = -y E \frac{d^2v}{dx^2}$$

Then we define that:

$$M = -\int_A \sigma_x dA = E \int_A y^2 \frac{d^2v}{dx^2} dA = EI \frac{d^2v}{dx^2}$$

$$K = \frac{M}{EI} = \frac{d^2v}{dx^2}$$

Therefore, we can get:

$$\int \sigma_x \varepsilon_x dV = \int \sigma_x \left(-y \frac{d^2v}{dx^2} \right) dV = \int_0^L \left(\int_A -y \sigma_x dA \right) \frac{d^2v}{dx^2} dx = \int_0^L MK dx$$

Now apply the principle of virtual work:

The equilibrium field is

$$\frac{d^2M^*}{dx^2} = -w^* \quad \frac{dM^*}{dx} = V^*$$

The compatible field is

$$\hat{K} = \frac{d^2 \hat{v}}{dx^2}$$

Thus we have:

$$\begin{aligned} \int_0^L M^* \hat{K} dx &= \int_0^L M^* \frac{d^2 \hat{v}}{dx^2} dx = [M^* \frac{d\hat{v}}{dx}]_0^L - \int_0^L \frac{dM^*}{dx} \frac{d\hat{v}}{dx} dx = [M^* \frac{d\hat{v}}{dx}]_0^L - [\frac{dM^*}{dx} \hat{v}]_0^L + \int_0^L \frac{d^2 M^*}{dx^2} \hat{v} dx \\ &= [M^* \frac{d\hat{v}}{dx}]_0^L - [V^* \hat{v}]_0^L + \int_0^L (-w^*) \hat{v} dx \\ &= M^*(L) \frac{d\hat{v}}{dx}(L) + (-M^*(0)) \frac{d\hat{v}}{dx}(0) + (-V^*(L)) \hat{v}(L) + V^*(0) \hat{v}(0) + \int_0^L (-w^*) \hat{v} dx \\ &= m_2^* \hat{\phi}_2 + m_1^* \hat{\phi}_1 + f_{2y}^* \hat{d}_{2y} + f_{1y}^* \hat{d}_{1y} + \int_0^L (-w^*) \hat{v} dx \end{aligned} \quad (10)$$

Where:

$$d_{1y} = v(0) \quad \phi_1 = \frac{dv}{dx}(0) \quad d_{2y} = v(L) \quad \phi_2 = \frac{dv}{dx}(L) \quad (\text{generalized displacement}) \quad (11)$$

$$f_{1y} = V(0) \quad m_1 = -M(0) \quad f_{2y} = -V(L) \quad m_2 = -M(L) \quad (\text{generalized forces}) \quad (12)$$

To attain the FEM formula, the interpolation polynomial for \hat{v} is given:

$$v(x) = a_0 + a_1 x + a_2 x^2 + a_3 x^3$$

In order to satisfy (11), the interpolation polynomial can be expressed in terms of d_{1y} , d_{2y} , ϕ_1 , ϕ_2

$$v(x) = d_{1y} N_1 + \phi_1 N_2 + d_{2y} N_3 + \phi_2 N_4$$

where N_1 to N_4 are the interpolation functions as shown in the Fig 2.3:

$$N_1 = 1 - 3 \left(\frac{x}{L}\right)^2 + 2 \left(\frac{x}{L}\right)^3$$

$$N_2 = x \left(1 - \frac{x}{L}\right)^2$$

$$N_3 = 3 \left(\frac{x}{L}\right)^2 - 2 \left(\frac{x}{L}\right)^3$$

$$N_4 = x \left\{ \left(\frac{x}{L}\right)^2 - \frac{x}{L} \right\}$$

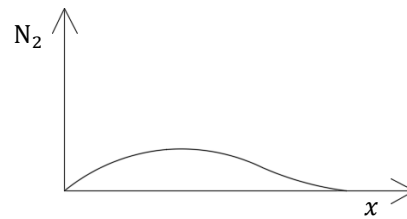
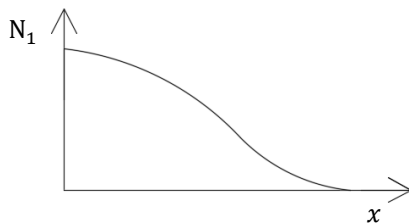




Fig 2.3 Interpolation functions

The first derivatives of the interpolation functions are:

$$N_1' = -\frac{6}{L^2}\hat{x} + \frac{6}{L^3}x^2$$

$$N_2' = 1 - \frac{4x}{L} + 3\left(\frac{x}{L}\right)^2$$

$$N_3' = \frac{6}{L}\hat{x} - \frac{6}{L^3}x^2 = -N_1'$$

$$N_4' = \frac{x}{L}\left(\frac{3x}{L} - 2\right)$$

The second derivatives of the interpolation functions are:

$$N_1'' = -\frac{6}{L^2}\left(1 - \frac{2x}{L}\right)$$

$$N_2'' = \frac{2}{L}\left(\frac{3x}{L} - 2\right)$$

$$N_3'' = -N_1'' = \frac{6}{L^2}\left(1 - \frac{2x}{L}\right)$$

$$N_4'' = \frac{2}{L}\left(\frac{3x}{L} - 1\right)$$

The third derivatives of the interpolation functions are:

$$N_1''' = \frac{12}{L^3} \quad N_2''' = \frac{6}{L^2} \quad N_3''' = -\frac{12}{L^3} \quad N_4''' = \frac{6}{L^2}$$

All the functions mentioned above fulfill the following condition:

$$N_1(0) = 1, \quad N_2(0) = N_3(0) = N_4(0) = 0$$

$$N_2'(0) = 1, \quad N_1'(0) = N_3'(0) = N_4'(0) = 0$$

$$N_3(L) = 1, \quad N_1(L) = N_2(L) = N_4(L) = 0$$

$$N_4'(L) = 1, \quad N_1'(L) = N_2'(L) = N_3'(L) = 0$$

$$\text{Let } (\Delta_1, \Delta_2, \Delta_3, \Delta_4) = (d_{y1}, \phi_1, d_{y2}, \phi_2) = \left(v(0), \frac{dv}{dx}(0), v(L), \frac{dv}{dx}(L) \right)$$

$$(Q_1, Q_2, Q_3, Q_4) = (f_{1y}, m_1, f_{2y}, m_2) = (V(0), -M(0), -V(L), M(L))$$

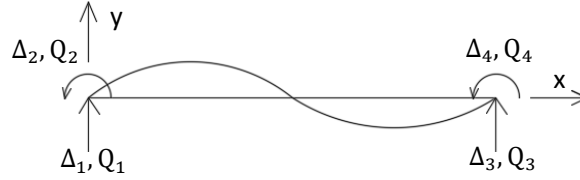


Fig 2.4 Generalized Displacement and Generalized Force

Select $v^* = \sum_{j=1}^4 \Delta_j N_j$ and $\hat{v} = N_i$ ($i = 1,2,3,4$) in (10) to get

$$\int_0^L EI \left(\sum_{j=1}^4 N_j \Delta_j \right)'' N_i'' dx = Q_i + \int_0^L (-w) N_i dx$$

Then it can be derived that

$$\sum_{j=1}^4 EI \left(\int_0^L N_j'' N_i'' dx \right) \Delta_j = Q_i + f_i$$

The equation can be expressed as:

$$\sum_{j=1}^4 K_{ji} \Delta_j = F_i$$

where

$$K_{ji} = EI \int_0^L N_j N_i'' dx$$

$$F_i = Q_i + f_i$$

$$f_1 = \int_0^L (-w) N_1(x) dx = -\frac{1}{2} wL$$

$$f_2 = \int_0^L (-w) N_2(x) dx = -\frac{1}{12} wL^2$$

$$f_3 = \int_0^L (-w) N_3(x) dx = -\frac{1}{2} wL$$

$$f_4 = \int_0^L (-w) N_4(x) dx = \frac{1}{12} wL^2$$

Here the matrix form of the stiffness matrix K_{ij} is:

$$\frac{2EI}{L^3} \begin{bmatrix} 6 & 3L & -6 & 3L \\ 3L & 2L^2 & -3L & L^2 \\ -6 & -3L & 6 & -3L \\ 3L & L^2 & -3L & 2L^2 \end{bmatrix}$$

In conclusion, the whole equation becomes

$$[K] \begin{bmatrix} \Delta_1 \\ \Delta_2 \\ \Delta_3 \\ \Delta_4 \end{bmatrix} = \begin{bmatrix} Q_1 \\ Q_2 \\ Q_3 \\ Q_4 \end{bmatrix} - \frac{1}{12} wL \begin{bmatrix} 6 \\ L \\ 6 \\ -L \end{bmatrix}$$

and

$$[K] \begin{bmatrix} d_{y1} \\ \phi_1 \\ d_{y2} \\ \phi_2 \end{bmatrix} = \begin{bmatrix} f_{1y} \\ m_1 \\ f_{2y} \\ m_2 \end{bmatrix} + \begin{bmatrix} -\frac{1}{2}wL \\ -\frac{1}{12}wL^2 \\ -\frac{1}{2}wL \\ \frac{1}{12}wL^2 \end{bmatrix}$$

After getting the stiffness matrix, we can now get the mass matrix by analyzing the dynamic Euler

Beam Element. The derivation process is given below.

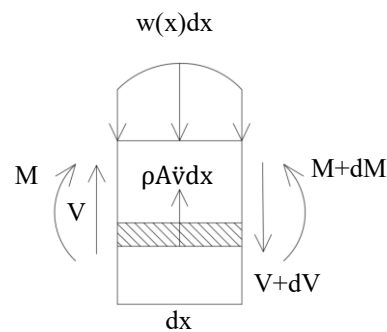


Fig 2.5 Dynamic Euler Beam Element

According to the Fig 2.4, we can have

$$-(V + dV) + V - wdx = \rho A \ddot{v} dx$$

$$M + dM - M - Vdx + wdx \frac{dx}{2} = 0$$

$$-\frac{dV}{dx} + w = -\rho A \ddot{v} \quad \frac{dM}{dx} = V$$

(13)

Apply the principle of virtual work

The equilibrium field is $\frac{dM^*}{dx} = V^*$, $\frac{dV^*}{dx} + w^* = -\rho A \ddot{v}$

The compatible Field is $\hat{K} = \frac{d^2\hat{v}}{dx^2}$

Therefore, we can obtain:

$$\begin{aligned}
\int_0^L M^* \hat{K} dx &= \int_0^L M^* \frac{d^2\hat{v}}{dx^2} dx = \left[M^* \frac{d\hat{v}}{dx} \right]_0^L - \int_0^L \frac{dM^*}{dx} \frac{d\hat{v}}{dx} dx = \left[M^* \frac{d\hat{v}}{dx} \right]_0^L - \left[\frac{dM^*}{dx} \hat{v} \right]_0^L + \int_0^L \frac{d^2M^*}{dx^2} \hat{v} dx \\
&= \left[M^* \frac{d\hat{v}}{dx} \right]_0^L - [V^* \hat{v}]_0^L + \int_0^L (-w^* - \rho A \ddot{v}^*) \hat{v} dx \\
&= \left[M^* \frac{d\hat{v}}{dx} \right]_0^L - [V^* \hat{v}]_0^L + \int_0^L (-w^*) \hat{v} dx - \int_0^L \rho A \ddot{v}^* \hat{v} dx \\
&= \sum_{k=1}^4 Q_k^* \hat{\Delta}_k + \int_0^L (-w^*) \hat{v} dx - \int_0^L \rho A \ddot{v}^* \hat{v} dx
\end{aligned} \tag{14}$$

To eventually get the FEM formulation, we substitute

$$v^* = \sum_{j=1}^4 \Delta_j N_j \quad \hat{v} = N_i \quad (i = 1, 2, 3, 4)$$

in (14) to get

$$\begin{aligned}
\int_0^L EI \left(\sum_{j=1}^4 N_j \Delta_j \right)'' N_i'' dx &= Q_i + \int_0^L (-w) N_i dx - \int_0^L \rho A \left(\sum_{j=1}^4 N_j \ddot{\Delta}_j \right) N_i dx \\
\sum_{j=1}^4 EI \left(\int_0^L N_j'' N_i'' dx \right) \Delta_j &= Q_i + f_i - \sum_{j=1}^4 \rho A \left(\int_0^L N_i N_j dx \right) \ddot{\Delta}_j \\
\sum_{j=1}^4 K_{ji} \Delta_j + \sum_{j=1}^4 M_{ji} \ddot{\Delta}_j &= Q_i + f_i
\end{aligned}$$

where

$$\begin{aligned}
K_{ji} &= EI \int_0^L N_j'' N_i'' dx \\
M_{ji} &= \rho A \int_0^L N_i N_j dx
\end{aligned}$$

The matrix form the achieved mass matrix is

$$M = \frac{\rho AL}{420} \begin{bmatrix} 156 & 22L & 54 & -13L \\ 22L & 4L^2 & 13L & -3L^2 \\ 54 & 13L & 156 & -22L \\ -13L & -3L^2 & -22L & 4L^2 \end{bmatrix}$$

2.2.1.3 Torsional Behavior

For 3-D Bernoulli Beam Element, only uniform torsion is considered. Assumptions for this behavior are [8]:

- 1) Cross sections are free to buckle.
- 2) Torsional resistance is only ensured by shear stress τ_{xy}, τ_{xz} active in the section's plane.

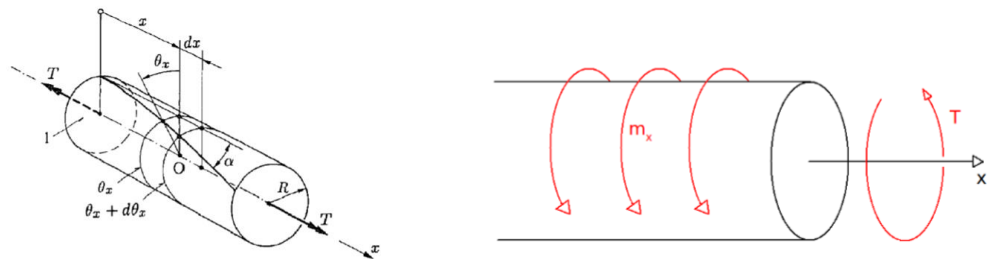


Fig 2.6 Torsional Behavior

Under the assumptions, we can have the following equations according to Saint-Venant torsion theory and uniform constitutive law.

$$\frac{d\theta}{dx} = X \quad (15)$$

$$T = GJX \quad (16)$$

where X is the torsion angle by unit length, θ_x is the torsion angle defined on figure, G is the shear modulus and J is a geometrical characteristic of the section called constant of torsion. [8]

The torsional equilibrium relation is written as [8]

$$\frac{dT}{dx} = -m_x \quad (17)$$

with m_x is the torsion moment by unit length.

(15), (16), (17) all together lead to the Torsional differential equation:

$$GJ \frac{d^2 \theta_x}{dx^2} + m_x = \rho J \ddot{\theta}_x$$

Get the weak form of the equation and substitute the interpolation functions: $\theta_x = \sum_{j=1}^2 \Delta_j \phi_j$, where

$$(\Delta_1, \Delta_2) = (\theta_{x1}, \theta_{x2}) \quad \phi_1 = 1 - \frac{(x-x_e)}{L} \quad \phi_2 = \frac{(x-x_e)}{L}$$

Then we can achieve the stiffness and mass matrix:

$$K_{ij} = \int_{x_e}^{x_{e+1}} GJ \frac{d\phi_i}{dx} \frac{d\phi_j}{dx} dx$$

$$K = \frac{GJ}{L} \begin{bmatrix} 1 & -1 \\ -1 & 1 \end{bmatrix}$$

$$M_{ij} = \int_{x_e}^{x_{e+1}} \rho J \phi_i \phi_j dx$$

$$M = \begin{bmatrix} \frac{\rho L}{3} & \frac{\rho L}{6} \\ \frac{\rho L}{6} & \frac{\rho L}{3} \end{bmatrix}$$

2.2.2 Thin (Kirchhoff) Plate Bending using BCIZ Triangular Element

The element we use in this section is based on the Kirchhoff plate theory. The Kirchhoff plate theory is also known as the classical plate theory (CPT). CPT is an extension of the Euler-Bernoulli beam theory from one dimension to two dimensions. It is based on the assumptions that a straight line perpendicular to the plane of the plate is (1) inextensible, (2) remains straight, and (3) rotates such that it remains perpendicular to the tangent to the deformed surface [11].

Detailed derivation of FEM formula is shown below.

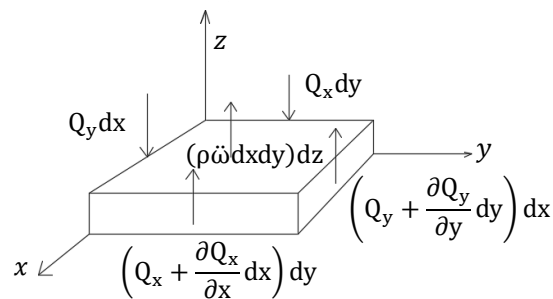


Fig 2.7 Motion on the Z-direction

As shown in the Fig 2.7, the equation of motion on z-direction is

$$\left(Q_x + \frac{\partial Q_x}{\partial x} dx\right) dy - Q_x dy + \left(Q_y + \frac{\partial Q_y}{\partial y} dy\right) dx - Q_y dx + p dx dy = \int_{-\frac{h}{2}}^{\frac{h}{2}} (\rho \ddot{\omega} dx dy) dz$$

where Q denotes the shear force, h denotes the thickness, ρ denotes the density and ω denotes the displacement in z -direction.

Divide it by $dx dy$ and we will have

$$\frac{\partial Q_x}{\partial x} + \frac{\partial Q_y}{\partial y} + p = \rho I_0 \ddot{\omega}$$

$$I_0 = \int_{-\frac{h}{2}}^{\frac{h}{2}} 1 dz = h$$

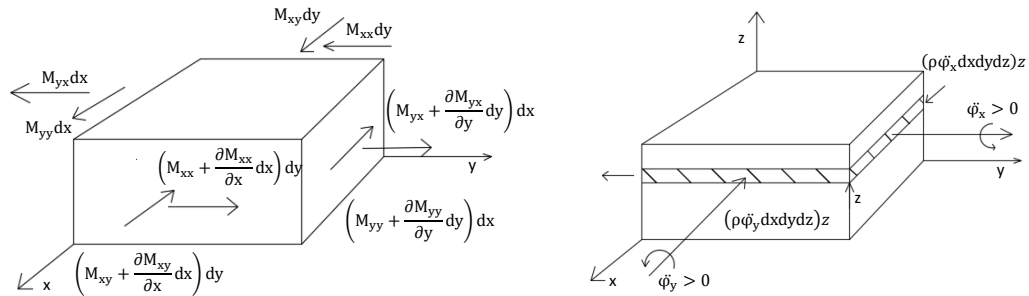


Fig 2.8 Moment about y axis and x axis

As seen in the Fig 2.8, the moment equilibrium about y axis is

$$\left(M_{yx} + \frac{\partial M_{yx}}{\partial y} dy\right) dx - M_{yx} dx + \left(M_{xx} + \frac{\partial M_{xx}}{\partial x} dx\right) dy - M_{xx} dy + Q_x dy dx = \int_{-\frac{h}{2}}^{\frac{h}{2}} z^2 (\rho \phi_x dx dy) dz$$

$$\frac{\partial M_{xx}}{\partial x} + \frac{\partial M_{yx}}{\partial y} - Q_x = \rho I_z \phi_x = -\rho I_z \frac{\partial^3 w}{\partial x \partial t^2}$$

$$\text{where } I_z = \int_{-\frac{h}{2}}^{\frac{h}{2}} z^2 dz \quad \partial_x = -\frac{\partial w}{\partial x} \quad \partial_y = \frac{\partial w}{\partial y} \quad (\text{w is the displacement in z-direction})$$

The moment equilibrium about x axis is

$$-\left(M_{yy} + \frac{\partial M_{yy}}{\partial y} dy\right) dx + M_{yy} dx - \left(M_{xy} + \frac{\partial M_{xy}}{\partial x} dx\right) dy - M_{xy} dy + Q_y dx dy = \int_{-\frac{h}{2}}^{\frac{h}{2}} z^2 (\rho \phi_y dx dy) dz$$

$$\frac{\partial M_{xy}}{\partial x} + \frac{\partial M_{yy}}{\partial y} - Q_y = -\rho I_z \frac{\partial^3 w}{\partial y \partial t^2}$$

Based on the equations above, we can now apply the principle of virtual work

The equilibrium field is:

$$\begin{aligned}\frac{\partial M_{xx}^*}{\partial x} + \frac{\partial M_{yx}^*}{\partial y} - Q_x^* &= -\rho I_z \frac{\partial^3 w^*}{\partial x \partial t^2} \\ \frac{\partial M_{xy}^*}{\partial x} + \frac{\partial M_{yy}^*}{\partial y} - Q_y^* &= -\rho I_z \frac{\partial^3 w^*}{\partial y \partial t^2} \\ \frac{\partial Q_x^*}{\partial x} + \frac{\partial Q_y^*}{\partial y} + p^* &= \rho I_0 \frac{\partial^2 w^*}{\partial t^2}\end{aligned}$$

The compatible field is

$$\widehat{K}_{\alpha\beta} = -\widehat{\omega}_{,\alpha\beta}$$

Therefore, we have:

$$\begin{aligned}\int \sigma_{\alpha\beta}^* \widehat{\varepsilon}_{\alpha\beta} dV &= \int_A dA \int_{-\frac{h}{2}}^{\frac{h}{2}} \sigma_{\alpha\beta}^* (-z \widehat{\omega}_{,\alpha\beta}) dz = \int_A dA \widehat{K}_{\alpha\beta} \int_{-\frac{h}{2}}^{\frac{h}{2}} z \sigma_{\alpha\beta}^* dz = \int_A M_{\alpha\beta}^* \widehat{K}_{\alpha\beta} dA \\ \int_A M_{\alpha\beta}^* \widehat{K}_{\alpha\beta} dA &= - \int_A M_{\alpha\beta}^* \widehat{\omega}_{,\alpha\beta} dA = - \int_c M_{\alpha\beta}^* \widehat{\omega}_{,\alpha} \nu_\beta ds + \int_A M_{\alpha\beta,\beta}^* \widehat{\omega}_{,\alpha} dA \\ &= \int_c M_s^* \widehat{\varphi}_s ds + \int_c M_{\alpha\beta,\beta}^* \widehat{\omega} \nu_\alpha ds - \int_A M_{\alpha\beta,\beta\alpha}^* \widehat{\omega} dA\end{aligned}$$

By using

$$\begin{cases} M_{\alpha\beta,\beta}^* - Q_\alpha^* = -\rho I_2 w_{,\alpha tt}^* \\ Q_{\alpha,\alpha}^* + p^* = -\rho I_0 w_{,tt}^* \end{cases}$$

we will have:

$$(M_{\alpha\beta,\beta}^* + \rho I_2 w_{,\alpha tt}^*)_{,\alpha} + p^* = \rho I_0 w_{,tt}^*$$

Additionally,

$$Q_n^* = Q_x^* \nu_x + Q_y^* \nu_y + \rho I_2 (\omega_{,xtt}^* \widehat{\omega}_{,x} \nu_x + \omega_{,ytt}^* \widehat{\omega}_{,y} \nu_y)$$

where Q_n^* denotes the normal shear force.

Then the equations become:

$$\begin{aligned}\int_c M_s^* \widehat{\varphi}_s ds + \int_c (Q_\alpha^* - \rho I_2 w_{,\alpha tt}^*) \widehat{\omega} \nu_\alpha ds + \int_A (\rho I_2 w_{,\alpha tt}^* + p^* - \rho I_0 w_{,tt}^*) \widehat{\omega} dA \\ = \int_c (M_s^* \widehat{\psi}_s + Q_n^* \widehat{\omega}) ds + \int_A -\rho I_2 w_{,\alpha tt}^* \widehat{\omega}_{,\alpha} + (p^* - \rho I_0 w_{,tt}^*) \widehat{\omega} dA\end{aligned}$$

We can convert the line integral term into:

$$\int_c (M_s^* \widehat{\psi}_s + Q_n^* \widehat{\omega}) ds = \int_c (M_n^* \widehat{\psi}_n + M_t^* \frac{\partial \widehat{\omega}}{\partial s} + Q_n^* \widehat{\omega}) ds$$

here

$$\int_c M_t^* \frac{\partial \widehat{w}}{\partial s} ds = \int_c \frac{\partial(M_t^* \widehat{w})}{\partial s} ds - \int_c \widehat{w} \frac{\partial M_t^*}{\partial s} ds = - \int_c \widehat{w} \frac{\partial M_t^*}{\partial s} ds$$

Substitute it into the original equation and then we will get

$$\int_c \{M_n^* \widehat{\psi}_n + (Q_n^* - \frac{\partial M_t^*}{\partial s}) \widehat{w}\} ds = \int_c \{-M_n^* \frac{\partial \widehat{w}}{\partial n} + Q_{\text{eff}}^* \widehat{w}\} ds$$

where

$$Q_n^* - \frac{\partial M_t^*}{\partial s} = Q_{\text{eff}}^*$$

$$\psi_n = - \frac{\partial \omega}{\partial n}$$

$$\psi_t = \frac{\partial \omega}{\partial s}$$

$$M_s \psi_s = M_n \psi_n + M_t \psi_t$$

are used.

Afterwards we can conclude that:

$$- \int_A M_{\alpha\beta}^* \widehat{w}_{,\alpha\beta} dA = \int_c \left\{ -M_n^* \frac{\partial \widehat{w}}{\partial n} + Q_{\text{eff}}^* \widehat{w} \right\} ds + \int_A -\rho I_2 w_{,\text{att}}^* \widehat{w}_{,\alpha} + (p^* - \rho I_0 w_{,\text{tt}}^*) \widehat{w} dA$$

Since the bending moments are as shown below [11]:

$$\begin{cases} M_{xx}^* = -(D_{11} \frac{\partial^2 w}{\partial x^2} + D_{12} \frac{\partial^2 w}{\partial y^2}) \\ M_{yy}^* = -(D_{12} \frac{\partial^2 w}{\partial x^2} + D_{22} \frac{\partial^2 w}{\partial y^2}) \\ M_{xy}^* = -2D_{66} \frac{\partial^2 w}{\partial x \partial y} \end{cases}$$

$$D_{11} = \frac{E_1 h^3}{12(1 - \nu_{12}\nu_{21})}, \quad D_{22} = \frac{E_2 h^3}{12(1 - \nu_{12}\nu_{21})}$$

$$D_{12} = \frac{\nu_{12} E_2 h^3}{12(1 - \nu_{12}\nu_{21})}, \quad D_{66} = \frac{G_{12} h^3}{12}$$

the equations become:

$$\begin{aligned} \int_A \rho I_2 w_{,\text{att}}^* \widehat{w}_{,\alpha} - (p^* - \rho I_0 w_{,\text{tt}}^*) \widehat{w} dA - \int_A M_{\alpha\beta}^* \widehat{w}_{,\alpha\beta} dA - \int_c \left\{ -M_n^* \frac{\partial \widehat{w}}{\partial n} + Q_{\text{eff}}^* \widehat{w} \right\} ds = 0 \\ \int_A \rho I_0 \widehat{w} \frac{\partial^2 w}{\partial t^2} + \rho I_2 \frac{\partial \widehat{w}}{\partial x} \frac{\partial^3 w}{\partial x \partial t^2} + \rho I_2 \frac{\partial \widehat{w}}{\partial y} \frac{\partial^3 w}{\partial y \partial t^2} + 4D_{66} \frac{\partial^2 w}{\partial x \partial y} \frac{\partial^2 \widehat{w}}{\partial x \partial y} + \left(D_{11} \frac{\partial^2 w}{\partial x^2} + D_{12} \frac{\partial^2 w}{\partial y^2} \right) \frac{\partial^2 \widehat{w}}{\partial x^2} \\ + \left(D_{12} \frac{\partial^2 w}{\partial x^2} + D_{22} \frac{\partial^2 w}{\partial y^2} \right) \frac{\partial^2 \widehat{w}}{\partial y^2} - p^* \widehat{w} dA - \int_c \left\{ -M_n^* \frac{\partial \widehat{w}}{\partial n} + Q_{\text{eff}}^* \widehat{w} \right\} ds = 0 \end{aligned}$$

$$\int_A \rho I_0 \hat{w} \frac{\partial^2 w}{\partial t^2} + \rho I_2 \left(\frac{\partial \hat{w}}{\partial x} \frac{\partial^3 w}{\partial x \partial t^2} + \frac{\partial \hat{w}}{\partial y} \frac{\partial^3 w}{\partial y \partial t^2} \right) + 4D_{66} \frac{\partial^2 w}{\partial x \partial y} \frac{\partial^2 \hat{w}}{\partial x \partial y} + \left(D_{11} \frac{\partial^2 w}{\partial x^2} + D_{12} \frac{\partial^2 w}{\partial y^2} \right) \frac{\partial^2 \hat{w}}{\partial x^2} + (D_{12} \frac{\partial^2 w}{\partial x^2} + D_{22} \frac{\partial^2 w}{\partial y^2}) \frac{\partial^2 \hat{w}}{\partial y^2} - p^* \hat{w} dA - \int_c \left\{ -M_n^* \frac{\partial \hat{w}}{\partial n} + Q_{\text{eff}}^* \hat{w} \right\} ds = 0 \quad (18)$$

To get the FEA formula of the plate element, we define the element nodal displacement as

$$d^T = \left\{ w_1, \left(\frac{\partial w}{\partial x} \right)_1, \left(\frac{\partial w}{\partial y} \right)_1, \omega_2, \left(\frac{\partial w}{\partial x} \right)_2, \left(\frac{\partial w}{\partial y} \right)_2, \omega_3, \left(\frac{\partial w}{\partial x} \right)_3, \left(\frac{\partial w}{\partial y} \right)_3 \right\}$$

And the interpolation functions of w and \hat{w} are

$$w = \Phi^T d = \sum_{j=1}^9 d_j \phi_j \quad \hat{w} = \phi_i (i = 1, 2, \dots, n)$$

where Φ is

$$\Phi^T = \{ \phi_{\omega 1}, \phi_{x1}, \phi_{y1}, \phi_{\omega 2}, \phi_{x2}, \phi_{y2}, \phi_{\omega 3}, \phi_{x3}, \phi_{y3} \}$$

The specific value Φ varies according to the element we choose during the analysis. Here, we select the BCIZ triangular element. It is an effective nonconforming triangular element developed by Bazeley, Cheung, Irons, and Zienkiewicz, and it consists of three degrees of freedom ($w, \frac{\partial w}{\partial x}, \frac{\partial w}{\partial y}$) at the three vertex nodes. The interpolation functions for the triangular element can be expressed in terms of area coordinates as

$$\begin{Bmatrix} \phi_{\omega 1} \\ \phi_{x1} \\ \phi_{y1} \\ \phi_{\omega 2} \\ \phi_{x2} \\ \phi_{y2} \\ \phi_{\omega 3} \\ \phi_{x3} \\ \phi_{y3} \end{Bmatrix} = \begin{Bmatrix} L_1 + L_1^2 L_2 + L_1^2 L_3 - L_2^2 L_1 - L_3^2 L_1 \\ x_{31}(L_3 L_1^2 - 0.5L_{123}) - x_{12}(L_2 L_1^2 + 0.5L_{123}) \\ y_{31}(L_3 L_1^2 + 0.5L_{123}) - y_{12}(L_2 L_1^2 + 0.5L_{123}) \\ L_2 + L_2^2 L_3 + L_2^2 L_1 - L_3^2 L_2 - L_1^2 L_2 \\ x_{12}(L_1 L_2^2 - 0.5L_{123}) - x_{23}(L_3 L_2^2 + 0.5L_{123}) \\ y_{12}(L_1 L_2^2 + 0.5L_{123}) - y_{23}(L_3 L_2^2 + 0.5L_{123}) \\ L_3 + L_3^2 L_1 + L_3^2 L_2 - L_1^2 L_3 - L_2^2 L_3 \\ x_{23}(L_2 L_3^2 - 0.5L_{123}) - x_{31}(L_1 L_3^2 + 0.5L_{123}) \\ y_{23}(L_2 L_3^2 + 0.5L_{123}) - x_{31}(L_1 L_3^2 + 0.5L_{123}) \end{Bmatrix}$$

where $L_{123} = L_1 L_2 L_3$ $x_{ij} = x_i - x_j$ $y_{ij} = y_i - y_j$, (x_i, y_i) being the global coordinates of the i th node.

Substitute the interpolation functions into the integration equation, then we can get:

$$[M^e] \{\ddot{d}^e\} + [K^e] \{d^e\} = \{F^e\} + \{Q^e\}$$

where the mass, stiffness and force matrix are as shown below:

$$M_{ij}^e = \int_A \left[\rho I_0 \phi_i \phi_j + \rho I_2 \left(\frac{\partial \phi_i}{\partial x} \frac{\partial \phi_j}{\partial x} + \frac{\partial \phi_i}{\partial y} \frac{\partial \phi_j}{\partial y} \right) \right] dA$$

$$K_{ij}^e = \int_A \left[D_{11} \frac{\partial^2 \phi_i}{\partial x^2} \frac{\partial^2 \phi_j}{\partial x^2} + D_{12} \left(\frac{\partial^2 \phi_i}{\partial x^2} \frac{\partial^2 \phi_j}{\partial y^2} + \frac{\partial^2 \phi_j}{\partial x^2} \frac{\partial^2 \phi_i}{\partial y^2} \right) + D_{22} \frac{\partial^2 \phi_i}{\partial y^2} \frac{\partial^2 \phi_j}{\partial y^2} + 4D_{66} \frac{\partial^2 \phi_i}{\partial x \partial y} \frac{\partial^2 \phi_j}{\partial x \partial y} \right] dA$$

$$F_i^e = \int_A p^* \phi_i dA \quad Q_i^e = \int_c \left(-M_n^* \frac{\partial \phi_i}{\partial n} + Q_{\text{eff}}^* \phi_i \right) ds$$

2.2.3 Allman Membrane Triangular Element

The Allman Membrane Triangular Element is a triangular finite element whose nodal degrees-of-freedom are two in-plane displacements and the 'drilling' rotation about a normal to the element plane developed by D.J Allman. The element is, essentially, an improvement of the standard constant strain triangle which was the first engineering application of the finite element method. [9,10]

This finite element model has cubic polynomial displacement fields u, v defined in terms of triangular co-ordinates (See Appendix A.1) L_1, L_2, L_3 over an arbitrary triangle with vertices P_1, P_2, P_3 , viz. [9]

$$\begin{aligned} u = & \left\{ \frac{1}{2}(\omega_1 + \omega_2) - \Omega_0 \right\} l_{12} \cos \gamma_{12} L_1 L_2 (L_2 - L_1) + \left\{ \frac{1}{2}(\omega_3 + \omega_2) - \Omega_0 \right\} l_{23} \cos \gamma_{23} L_3 L_2 (L_3 - L_2) \\ & + \left\{ \frac{1}{2}(\omega_1 + \omega_3) - \Omega_0 \right\} l_{31} \cos \gamma_{31} L_1 L_3 (L_1 - L_3) + \frac{1}{2}(\omega_2 - \omega_1) l_{12} \cos \gamma_{12} L_1 L_2 \\ & + \frac{1}{2}(\omega_3 - \omega_2) l_{23} \cos \gamma_{23} L_2 L_3 + \frac{1}{2}(\omega_1 - \omega_3) l_{31} \cos \gamma_{31} L_3 L_1 + u_1 L_1 + u_2 L_2 + u_3 L_3 \\ v = & \left\{ \frac{1}{2}(\omega_1 + \omega_2) - \Omega_0 \right\} l_{12} \sin \gamma_{12} L_1 L_2 (L_2 - L_1) + \left\{ \frac{1}{2}(\omega_3 + \omega_2) - \Omega_0 \right\} l_{23} \sin \gamma_{23} L_3 L_2 (L_3 - L_2) \\ & + \left\{ \frac{1}{2}(\omega_1 + \omega_3) - \Omega_0 \right\} l_{31} \sin \gamma_{31} L_1 L_3 (L_1 - L_3) + \frac{1}{2}(\omega_2 - \omega_1) l_{12} \sin \gamma_{12} L_1 L_2 \\ & + \frac{1}{2}(\omega_3 - \omega_2) l_{23} \sin \gamma_{23} L_2 L_3 + \frac{1}{2}(\omega_1 - \omega_3) l_{31} \sin \gamma_{31} L_3 L_1 + u_1 L_1 + u_2 L_2 + u_3 L_3 \end{aligned}$$

where l_{ij} ($ij = 12, 23, 31$) are the lengths of the three sides whose outward normals are inclined at angles γ_{ij} to the x -axis. ω_i ($i = 1, 2, 3$) are vertex rotational degrees-of-freedom and where Ω_0 is the rotation

of the constant strain triangle of area A expressed in terms of its nodal degrees-of-freedom u_i , v_i and nodal co-ordinates x_i , y_i , viz. [9]

$$\Omega_0 = \frac{1}{4A} [(x_2 - x_3)u_1 + (x_3 - x_1)u_2 + (x_1 - x_2)u_3 + (y_2 - y_3)v_1 + (y_3 - y_1)v_2 + (y_1 - y_2)v_3]$$

Then we convert the displacement equations into

$$\begin{Bmatrix} u \\ v \end{Bmatrix} = NU = \begin{Bmatrix} N_u \\ N_v \end{Bmatrix} U$$

where

$$U = \{u_1, v_1, w_1, u_2, v_2, w_2, u_3, v_3, w_3\}$$

$$N_u = \left[L_1 - \frac{V_{co}}{4A} b_1 \quad \frac{V_{co}}{4A} a_1 \quad w_{c1} \quad L_2 - \frac{V_{co}}{4A} b_2 \quad \frac{V_{co}}{4A} a_2 \quad w_{c2} \quad L_3 - \frac{V_{co}}{4A} b_3 \quad \frac{V_{co}}{4A} a_3 \quad w_{c3} \right]$$

$$N_v = \left[-\frac{V_{so}}{4A} b_1 \quad L_1 + \frac{V_{so}}{4A} a_1 \quad w_{s1} \quad -\frac{V_{so}}{4A} b_2 \quad L_2 + \frac{V_{so}}{4A} a_2 \quad w_{s2} \quad -\frac{V_{so}}{4A} b_3 \quad L_3 + \frac{V_{so}}{4A} a_3 \quad w_{s3} \right]$$

with

$$V_{co} = -\{l_{12} \cos \gamma_{12} L_1 L_2 (L_2 - L_1) + l_{23} \cos \gamma_{23} L_2 L_3 (L_3 - L_2) + l_{31} \cos \gamma_{31} L_3 L_1 (L_1 - L_3)\}$$

$$V_{so} = V_{co}(\cos \rightarrow \sin)$$

and

$$w_{c1} = \frac{1}{2} \{l_{12} \cos \gamma_{12} L_1 L_2 (L_2 - L_1) + l_{31} \cos \gamma_{31} L_3 L_1 (L_1 - L_3) + l_{31} \cos \gamma_{31} L_3 L_1 - l_{12} \cos \gamma_{12} L_1 L_2\}$$

$$w_{c2} = \frac{1}{2} \{l_{12} \cos \gamma_{12} L_1 L_2 (L_2 - L_1) + l_{23} \cos \gamma_{23} L_2 L_3 (L_3 - L_2) + l_{12} \cos \gamma_{12} L_1 L_2 - l_{23} \cos \gamma_{23} L_2 L_3\}$$

$$w_{c3} = \frac{1}{2} \{l_{23} \cos \gamma_{23} L_2 L_3 (L_3 - L_2) + l_{31} \cos \gamma_{31} L_3 L_1 (L_1 - L_3) + l_{23} \cos \gamma_{23} L_2 L_3 - l_{31} \cos \gamma_{31} L_3 L_1\}$$

$$w_{si} = w_{ci}(\cos \rightarrow \sin)$$

The stress and strain fields are

$$\begin{cases} \varepsilon_x = \frac{\partial u}{\partial x} \\ \varepsilon_y = \frac{\partial v}{\partial y} \\ \gamma_{xy} = \frac{\partial v}{\partial x} + \frac{\partial u}{\partial y} \end{cases}$$

$$\varepsilon = BU$$

Substitute the displacement equations into these stress and strain equations and we will have the matrix

B. The non-linear part of the matrix is

B(Non – Linear)

$$= \frac{1}{2A} \begin{bmatrix} \frac{b_1}{4A}f(c, a) & -\frac{a_1}{4A}f(c, a) & \frac{1}{2}g_1(c, a) & \frac{b_2}{4A}f(c, a) & -\frac{a_2}{4A}f(c, a) & \frac{1}{2}g_2(c, a) & \frac{b_3}{4A}f(c, a) & -\frac{a_3}{4A}f(c, a) & \frac{1}{2}g_3(c, a) \\ \frac{b_1}{4A}f(s, b) & -\frac{a_1}{4A}f(s, b) & \frac{1}{2}g_1(s, b) & \frac{b_2}{4A}f(s, b) & -\frac{a_2}{4A}f(s, b) & \frac{1}{2}g_2(s, b) & \frac{b_3}{4A}f(s, b) & -\frac{a_3}{4A}f(s, b) & \frac{1}{2}g_3(s, b) \\ \frac{b_1}{4A}f(c, a) & [-\frac{a_1}{4A}f(c, a)] & [\frac{1}{2}g_1(c, a)] & \frac{b_2}{4A}f(c, a) & [-\frac{a_2}{4A}f(c, a)] & [\frac{1}{2}g_2(c, a)] & \frac{b_3}{4A}f(c, a) & [-\frac{a_3}{4A}f(c, a)] & [\frac{1}{2}g_3(c, a)] \\ +\frac{b_1}{4A}f(s, b) & -\frac{a_1}{4A}f(s, b) & +\frac{1}{2}g_1(s, b) & +\frac{b_2}{4A}f(s, b) & -\frac{a_2}{4A}f(s, b) & +\frac{1}{2}g_2(s, b) & +\frac{b_3}{4A}f(s, b) & -\frac{a_3}{4A}f(s, b) & +\frac{1}{2}g_3(s, b) \end{bmatrix}$$

The function f and g are defined as shown below

$$f(c, a) = (l_{31}c_{31}a_3 - l_{12}c_{12}a_2)L_1^2 + (l_{12}c_{12}a_1 - l_{23}c_{23}a_3)L_2^2 + (l_{23}c_{23}a_2 - l_{31}c_{31}a_1)L_3^2 \\ + 2l_{12}c_{12}(a_2 - a_1)L_1L_2 + 2l_{23}c_{23}(a_3 - a_2)L_2L_3 + 2l_{31}c_{31}(a_1 - a_3)L_3L_1$$

$$\begin{cases} f(s, b) & (c, a) \rightarrow (s, b) \\ f(c, b) & (c, a) \rightarrow (c, b) \\ f(s, a) & (c, a) \rightarrow (s, a) \end{cases}$$

$$g_i(c, a) = (l_{ij}c_{ij}a_i - l_{ij}c_{ij}a_j)(L_i^2 + L_j) + l_{ij}c_{ij}a_i(L_j^2 - L_j) - l_{ij}c_{ij}a_i(L_i^2 - L_i) + 2l_{ij}c_{ij}(a_j - a_i)L_iL_j \\ + 2l_{ij}c_{ij}(a_i - a_j)L_iL_j$$

$$\text{where} \quad (i, j, l) = \begin{cases} 1, 2, 3 & (i = 1) \\ 2, 3, 1 & (i = 2) \\ 3, 1, 2 & (i = 3) \end{cases}$$

$$\begin{cases} g_i(s, b) & (c, a) \rightarrow (s, b) \\ g_i(c, b) & (c, a) \rightarrow (c, b) \\ g_i(s, a) & (c, a) \rightarrow (s, a) \end{cases}$$

The linear part of the matrix B is

$$B(\text{Linear}) = \begin{bmatrix} a_1 & 0 & 0 & a_2 & 0 & 0 & a_3 & 0 & 0 \\ 0 & b_1 & 0 & 0 & b_2 & 0 & 0 & b_3 & 0 \\ b_1 & a_1 & 0 & b_2 & a_2 & 0 & b_3 & a_3 & 0 \end{bmatrix}$$

Matrix B is the sum of the two parts,

$$B = B(\text{Non – Linear}) + B(\text{Linear})$$

With the obtained equations in the preceding paragraphs, we can eventually achieve the stiffness matrix, mass matrix and the load vector, of which the process is shown below:

The stiffness matrix is defined as:

$$K_e = \iint_A B^T D B t dx dy = \iint_A \bar{K} t dx dy$$

here t is the element thickness.

$$D = \frac{E}{1-\nu^2} \begin{bmatrix} 1 & \nu & 0 \\ \nu & 1 & 0 \\ 0 & 0 & \frac{1-\nu}{2} \end{bmatrix}$$

$$\bar{K}_{ij} = \frac{E}{1-\nu^2} \left\{ B_{1i} B_{1j} + B_{2i} B_{2j} + \nu (B_{2i} B_{1j} + B_{1i} B_{2j}) + \frac{1-\nu}{2} B_{3i} B_{3j} \right\}$$

where E is the Young's Modulus and ν is the Poisson's ratio of the element.

The mass matrix is

$$M = \iint_A \rho t N_u^T N_u dA + \iint_A \rho t N_v^T N_v dA$$

To get the element load vector, we first need to have the normal & tangential displacement along $P_i P_j$

$$\begin{cases} u_n(s) = A_{ij} s \left(1 - \frac{s}{l_{ij}} \right) \left(2 \frac{s}{l_{ij}} - 1 \right) + B_{ij} s \left(1 - \frac{s}{l_{ij}} \right) + \left(1 - \frac{s}{l_{ij}} \right) u_{ni} + \left(\frac{s}{l_{ij}} \right) u_{nj} \\ u_t(s) = \left(1 - \frac{s}{l_{ij}} \right) u_{ti} + \left(\frac{s}{l_{ij}} \right) u_{tj} \end{cases}$$

The associated potential energy is

$$V_{ij}^{(1)} = - \int_{P_i P_j} (\sigma_n u_n + \tau_t u_t) t ds$$

Assume σ_n and τ_t to be constant and use

$$u_n(s) = \frac{1}{2} s \left(1 - \frac{s}{l_{ij}} \right) (\omega_j - \omega_i) + \left(1 - \frac{s}{l_{ij}} \right) u_{ni} + \left(\frac{s}{l_{ij}} \right) u_{nj}$$

$$u_t(s) = \left(1 - \frac{s}{l_{ij}} \right) u_{ti} + \left(\frac{s}{l_{ij}} \right) u_{tj}$$

Then we will have

$$V_{ij}^1 = \{u_{ni}, u_{ti}, \omega_i, u_{nj}, u_{tj}, \omega_j\} \left\{ \begin{array}{c} \frac{1}{2} \sigma_n t l_{ij} \\ \frac{1}{2} \tau_t t l_{ij} \\ -\frac{1}{12} \sigma_n t l_{ij}^2 \\ \frac{1}{2} \sigma_n t l_{ij} \\ \frac{1}{2} \tau_t t l_{ij} \\ \frac{1}{12} \sigma_n t l_{ij}^2 \end{array} \right\}$$

For the constant distributions of body force X^* , Y^* , the associated potential energy is

$$V^2 = - \iint_A (X^* u + Y^* v) t dx dy$$

where

$$u = \frac{1}{2} (\omega_2 - \omega_1) l_{12} \cos \gamma_{12} L_1 L_2 + \frac{1}{2} (\omega_3 - \omega_2) l_{23} \cos \gamma_{23} L_2 L_3 + \frac{1}{2} (\omega_1 - \omega_3) l_{31} \cos \gamma_{31} L_3 L_1 + u_1 L_1 \\ + u_2 L_2 + u_3 L_3$$

$$v = \frac{1}{2} (\omega_2 - \omega_1) l_{12} \sin \gamma_{12} L_1 L_2 + \frac{1}{2} (\omega_3 - \omega_2) l_{23} \sin \gamma_{23} L_2 L_3 + \frac{1}{2} (\omega_1 - \omega_3) l_{31} \sin \gamma_{31} L_3 L_1 + u_1 L_1 \\ + u_2 L_2 + u_3 L_3$$

The total potential energy of the applied force is:

$$V = V^1 + V^2$$

Where γ is the angle between x axis of the global coordination and the first beam element*.

(*here the first beam element means the beam between Node1 and Node2)

2.3.3 Assembly of Allman Shell Element with drilling degree of freedom

The Allman Shell Element is constructed with the Allman's Membrane Element and the Plate Bending Element. The Stiffness and Mass Matrix of the shell element is the combination of the stiffness and mass matrices of the membrane and plate bending element, which are derived in the previous sections.

2.3.4 Transform in to Global Coordination

Transform the 3D Euler-Bernoulli Beam element and the Allman Shell Element into global coordination by the transform matrix as the following 18×18 matrix:

$$T = \begin{bmatrix} \Lambda & \cdots & \\ \vdots & \ddots & \vdots \\ & \cdots & \Lambda \end{bmatrix} \quad \Lambda = \begin{bmatrix} \hat{u} \\ \hat{v} \\ \hat{w} \end{bmatrix}$$

where \hat{u} , \hat{v} , \hat{w} are the unit vectors of the x-axis, y-axis and z-axis, respectively, of the local coordination of the triangle element.

2.3.5 Assembly of Allman Stiffened Shell Element

Add the transformed stiffness matrices, as well as the mass matrices, of the frame element and shell element together respectively to stiffen the edge of the shell element with the triangle frame. Now we have the final stiffness and mass matrices of the Allman Stiffened Shell Element and we are able to calculate the natural frequencies of the element. The linear eigenvalue problem equation of structural dynamics is

$$\lambda KD = MD$$

Here, λ denotes the eigenvalue and the D is a vector whose components are the global degrees of freedom.

2.3.6 The Matlab Code

A Matlab Code is developed based on the equations derived above and we can now analyze the effects of veins on the insect wing structure by calculating the structure's natural frequencies and eigenmodes under different problem settings.

Chapter Three

Numerical Examples

3.1 Finite Element Modelling

To explore how vein arrangement contributes to the performance of insect wing structures, a finite element model is created. The geometry and material properties of the model is partially based on the *Manduca Sexta*, a moth of family Sphingidae that constantly used as an example for MAV design. The model is highly simplified since our goal is not to replicate the wing of a specific kind of insect, but rather to create a general model of a wing to see how the change of vein distribution affects the overall performance of the structure. As you can see in the Fig3.1, the model is a flat stiffened triangle shell of uniform thickness, composed of 130 stiffened shell elements.

The left end of the structure is where the wing is connected to the body and here it is called the supporting point. The horizontal edge of the wing is the leading edge and the other edge passing through the supporting point is the trailing edge. The edge which is opposite to the supporting point is called the side edge. The wing can be divided by the red line into two parts. Here we call the part left to the red line the proximal part and the part right to it the remote part. Additionally, a Cartesian coordination system is established for the analysis, of which the origin is located at the supporting point and the x-axis is along the leading edge of the wing. The y-axis of the system is vertical to the leading edge and points downwards and the z-axis points outwards.

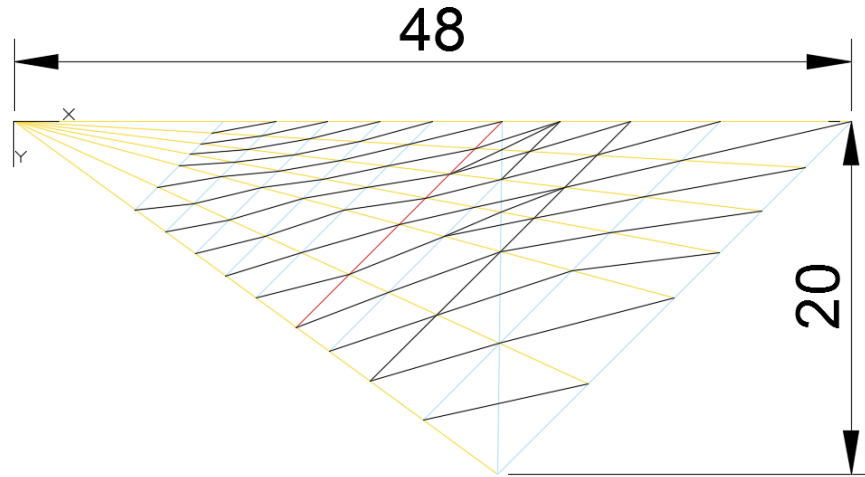


Fig3.1: The General Wing Model based on Manduca Sexta

Table3.1 summarizes the geometry and material properties of the wing model, such as thickness, Poisson's Ratio, density etc. The detailed information of each node is listed in the Appendix A.2

Span Length (mm)	Chord Length(mm)	Thickness(μm)
48	20	12
Young's Modulus (GPa)	Poisson's Ratio	Density(g/cm^3)
1.90	0.495	2.30

Table 3.1 Properties of the General Wing Model

3.2 Experimental Cases

Various experimental cases are implemented during the test. The veins of the wing structure are represented by the beam elements on the edge of the shell element. By changing the distribution of the beam elements, we can obtain different arrangements of veins.

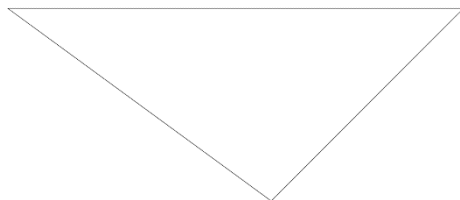
In this test, all the veins share the same cross-section and the same material properties, which are shown in the Table3.2.

Length(μm)	Width(μm)	Density(g/cm^3)
30	30	1.40
Young's Modulus (GPa)	Poisson's Ratio	
4.00	0.495	

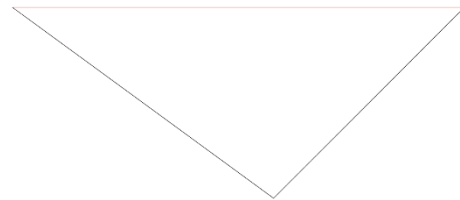
Table 3.2 Properties of the Veins

3.2.1 Case Set 1: Longitudinal Vein Arrangements

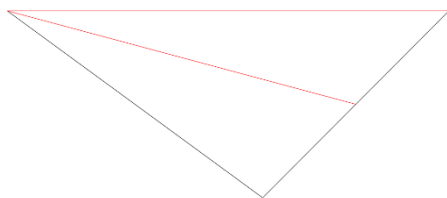
The first set contains five cases that focus on the effects of the longitudinal veins, which are also known as radiating veins. It should be noted that the longitudinal veins are originated from the proximal supporting point, where the wing and the insect body are connected together, and distributed in the radial direction. As shown in Fig 3.2, Case 1 is the wing structure without any vein, so that it can be used as a reference for the following tests. In Case 2, the red line indicates the vein added to the leading edge of the wing structure. The middle longitudinal vein, which connects the supporting point and the middle point of the opposite edge, is added to the structure in the Case 3. The opposite edge is now divided into two parts by the middle vein. The two parts are called the upper part and the lower part respectively. Two more veins that connect the middle points of each part and the supporting point are added in the Case 4. In Case 5, the first quarter point and the third quarter point of the upper part are connected by the added longitudinal veins.



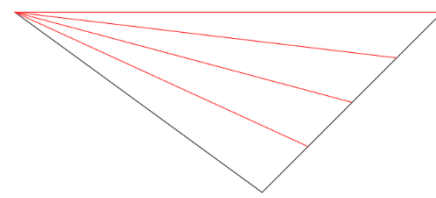
Case 1



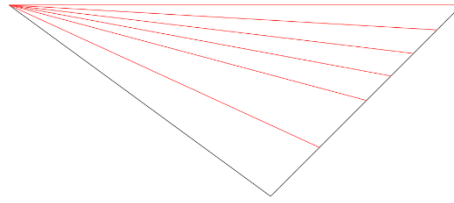
Case 2



Case 3



Case 4

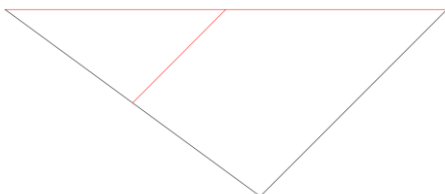


Case 5

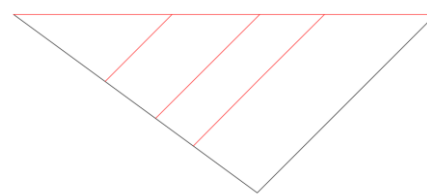
Fig 3.2 Case Set 1

3.2.2 Case Set 2: Cross Vein Arrangements

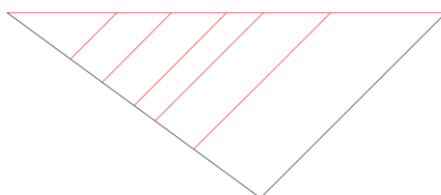
The second set also contains five cases, but this time it mainly focuses on the effect of the cross veins. In this case, all the cross veins are parallel to the side edge which is opposite to the supporting point. Similarly, in the Case 6, the first cross vein added to the structure is the middle cross vein that connected the middle points of the leading edge and the trailing edge. As we can see in the Fig 3.3, more cross veins are added to both the left and right side of the middle vein in the following cases, by which means we can explore the effects of adding cross veins in either closer or farther positions to the supporting point. Additionally, the cross veins on the left side of the middle vein are evenly distributed while the distance between the veins on the right side is slightly increasing from the left to the right.



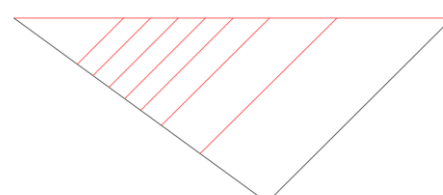
Case 6



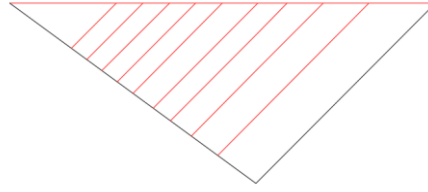
Case 7



Case 8



Case 9

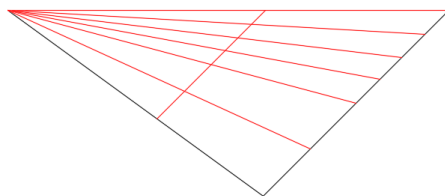


Case 10

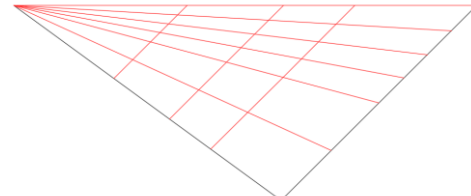
Fig 3.3 Case Set 2

3.2.3 Case Set 3: Combined Veins Arrangements

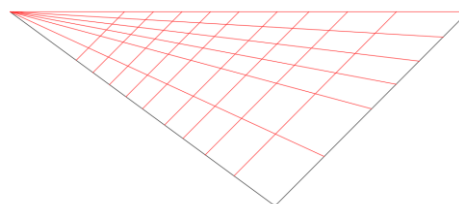
The third set contains three cases which include different combined arrangements of longitudinal veins and cross veins. If we take a closer look to these cases, we can find that all the three cases are composed of the cases in previous Case Sets. Case 11 is the combination of Case 5 and Case 6, while the Case 12 is the combination of Case 5 and Case 7. Case 13, the final test case, is the combination of Case 5 and Case 10.



Case 11



Case 12



Case 13

Fig 3.4 Case Set 3

3.3 Numerical Performance

The numerical performance of the cases is achieved by using the Matlab Code mentioned in the Chapter 2. The general boundary condition of the tests is that the left end of the wing is fixed in all six

degrees of freedom. For each case, more than 400 natural frequencies and the corresponding modeshapes, that is, how the structure responds to a certain natural frequency, are obtained. Thus we can have a clear picture of the relationship between vein arrangements and the performance of wing structure. Here the analysis only concerns the six dominant modeshapes at low-frequencies of each case due to the limitation of time and energy.

3.3.1 The Reference Case

Case 1 includes an unstiffened wing structure, of which results are used as a reference for the following tests. As shown in the Figure 3.5, the six dominant natural frequencies of Case 1 ranges from 3.173 Hz to 167 Hz.

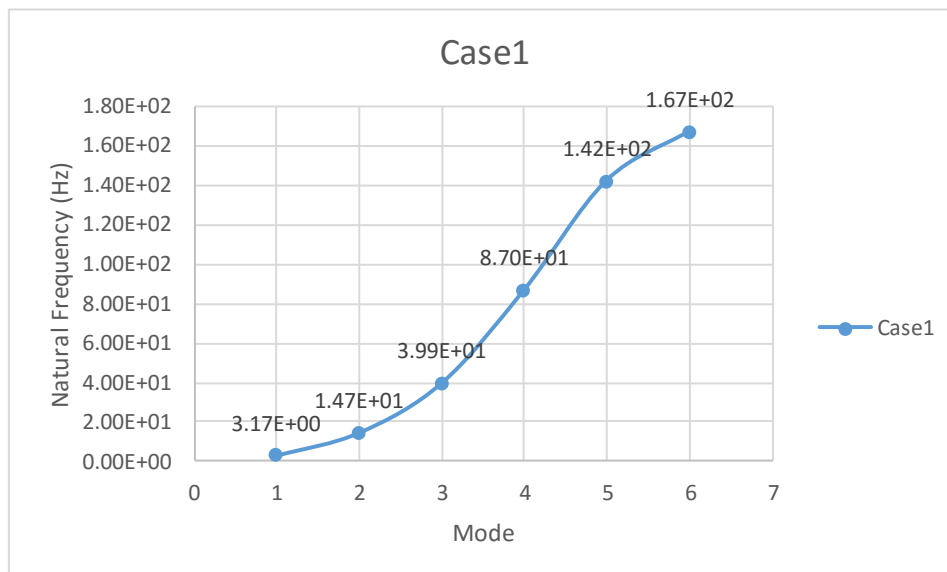
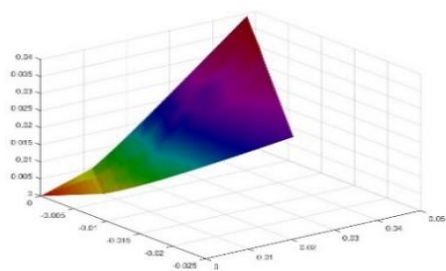
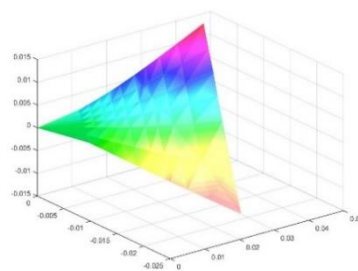
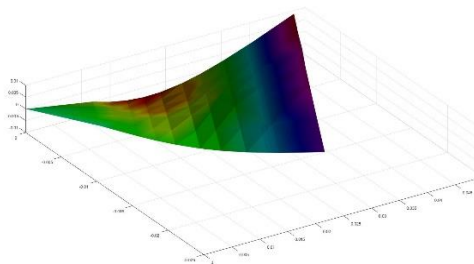
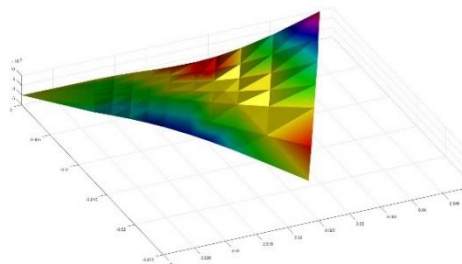
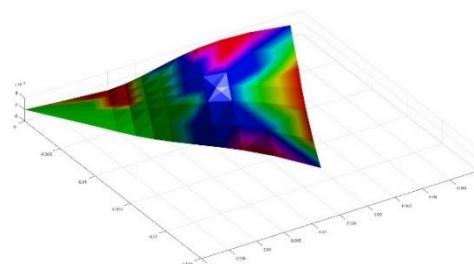
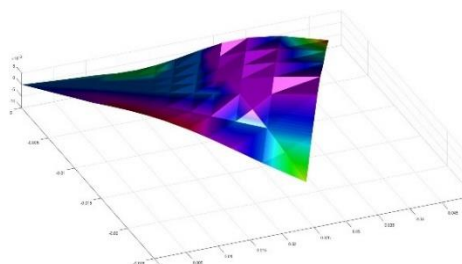


Fig 3.5 Natural Frequencies of Case 1

According to the obtained analysis results, the deformation of wing structure under low frequency consists of displacement in the z-direction, rotation about x-axis and rotation about y-axis. To illustrate the results more clearly, the graphs of corresponding modeshapes are drawn according to the obtained displacement values and shown in the Fig 3.6.

**Mode 1****Mode 2****Mode 3****Mode 4****Mode 5****Mode 6****Fig 3.6 Modeshapes of Case 1 【Color Denotes the Displacement】**

As we can see in the figure, the first modeshape is the bending mode and second modeshape is the torsion mode, which happens under 3.173 Hz and 14.73Hz, respectively. The bending mode is along the y-direction, while the central axis of the torsion mode is near to the central line that connects the supporting node and the middle point of the side edge. Both the third and the fourth modeshape are composed of bending and torsion motion. The difference between these two similar modes is that the torsion in the third mode takes place in the proximal part, which near to the supporting point of the wing, while, in the fourth mode, it occurs at the remote part that is near to the wing tip. The fifth modeshape is the so-called “saddle mode”. It can be observed that the deflections on both the leading and trailing edges

and the deflection on the side edge together form a saddle-like shape. Other than that, it also includes two bending motions and torsion in the proximal part of the wing. Mode 6 occurs at a slightly higher frequency than Mode 5. In Mode 6, the deflections seen in Mode 5 move from the edges to the wing tips and the torsion becomes more notable.

3.3.2 Effects of the Longitudinal Veins Arrangements

3.3.2.1 Effects on the Natural Frequencies

From Case 2 to Case 5, various vein arrangements are introduced to the wing structure. The six dominant natural frequencies of each case are shown in the Table 3.3. Here, the obtained values are compared with the values of the reference case and the increment percentages of natural frequency due to the changes of arrangement are shown in the Table 3.4. Fig 3.7 shows the change of natural frequencies for each Mode from Case 2 to Case 5.

	Case1	Case2	Case3	Case4	Case5
Mode1	3.17E+00	3.545	3.878	4.452	4.958
Mode2	1.47E+01	1.55E+01	1.61E+01	1.75E+01	1.85E+01
Mode3	3.99E+01	4.23E+01	4.39E+01	4.69E+01	5.02E+01
Mode4	8.70E+01	8.94E+01	9.13E+01	9.51E+01	9.89E+01
Mode5	1.42E+02	1.47E+02	1.50E+02	1.56E+02	1.61E+02
Mode6	1.67E+02	1.74E+02	1.76E+02	1.82E+02	1.91E+02

Table 3.4 Natural Frequencies of Case 1 to 5

	Case1	Case2	Case3	Case4	Case5
Mode1	100%	110.58%	122.33%	140.31%	156.26%
Mode2	100%	104.89%	109.57%	118.47%	125.87%
Mode3	100%	106.12%	110.06%	117.54%	125.84%
Mode4	100%	102.75%	104.92%	109.26%	113.63%
Mode5	100%	103.46%	105.63%	109.70%	113.01%
Mode6	100%	104.08%	105.39%	109.16%	114.25%

Table 3.5 Increment Percentages of Natural Frequencies

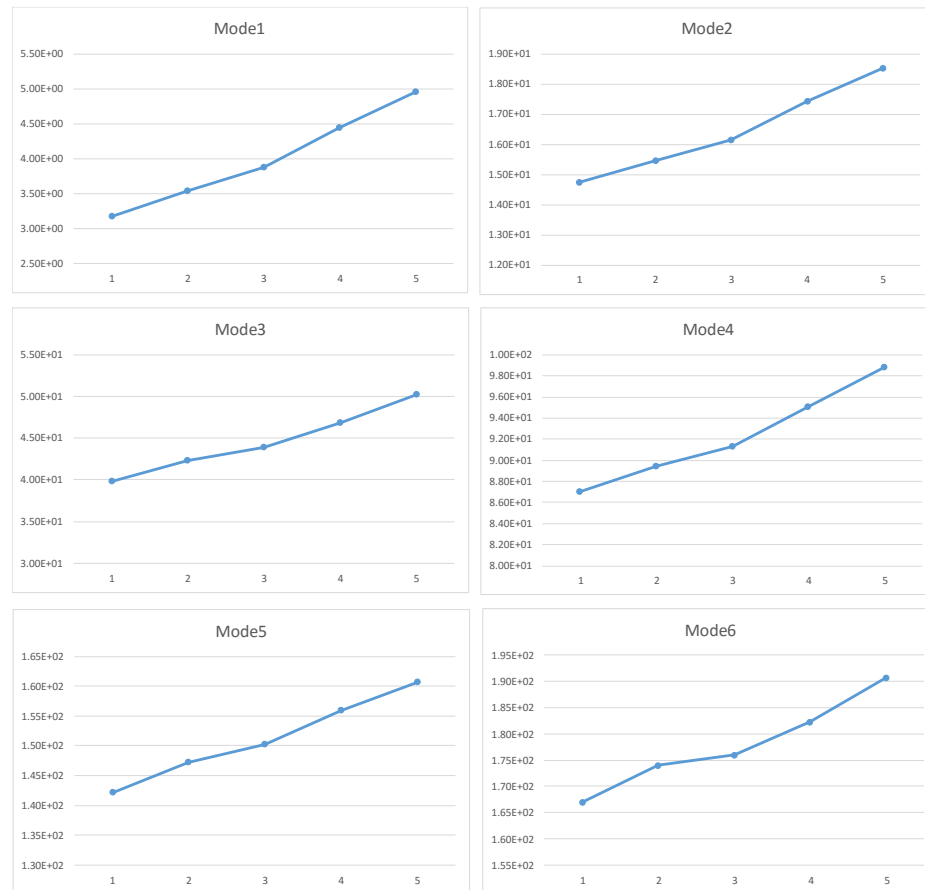


Fig 3.7 The change of corresponding natural frequencies for each mode.

By examining the results of four cases, one can easily find that adding longitudinal veins to the structure dramatically increases the natural frequencies of Mode 1. It is justified to assume that such change is due to the fact that adding longitudinal veins increase the stiffness of the whole structure in the radius direction and make it more resistible to the bending motion along y-axis. The average increment is around 9.38% for each added vein. The increment of frequency by adding longitudinal veins near the central line is a little bit higher than the increment by adding veins to the leading edges. Along with the increase of numbers of longitudinal veins added to the structure, the frequency increment due to each added vein is decreasing.

Similar tendency can also be observed in other modes, but with less increment. The average increments of Case 2 and Case 3 are both around 4.3%. Meanwhile, the average increments of rest cases are around 2.2%. Thus we can come to a conclusion that the most significant effect of adding longitudinal veins to

the natural frequencies is on the first modeshape, that is, the pure bending mode. For other modes which consist of not only bending motion, but also torsion and various deflections, the effect of adding veins becomes less considerable.

3.3.2.2 Effects on the Modeshapes

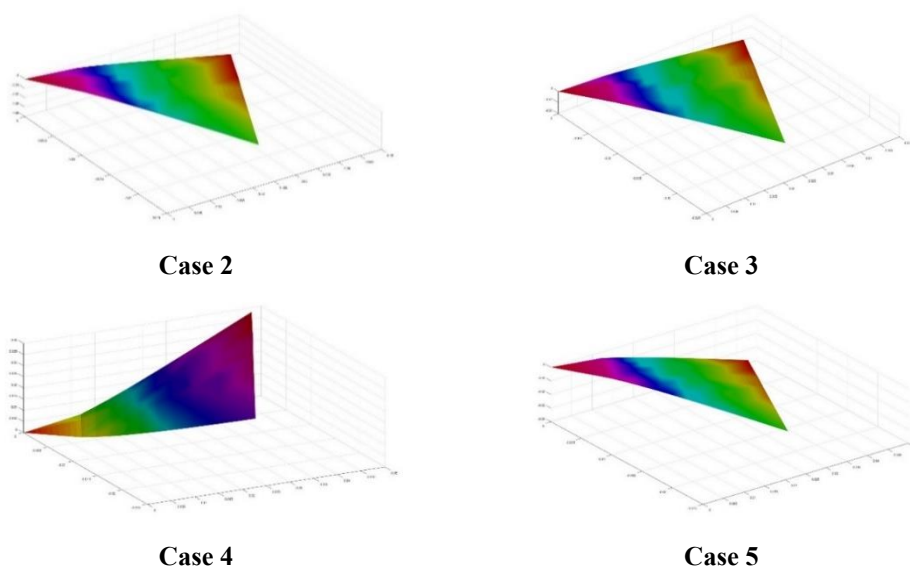
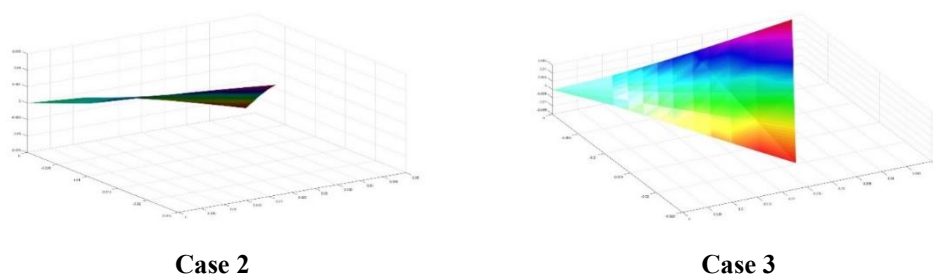


Fig 3.8 Mode 1 a) Case 2 ~ 5 b) Color bands denote displacement

Fig 3.8 shows the change of mode 1 under different longitudinal vein arrangements. As shown in the figure, adding longitudinal veins doesn't change the type of motion, despite that the wing bends in the reverse direction in Case 4. However, the node displacement in z-direction slightly decrease along with the increase of number of veins added to the wing structure, which strengthens the stiffness of the structure.



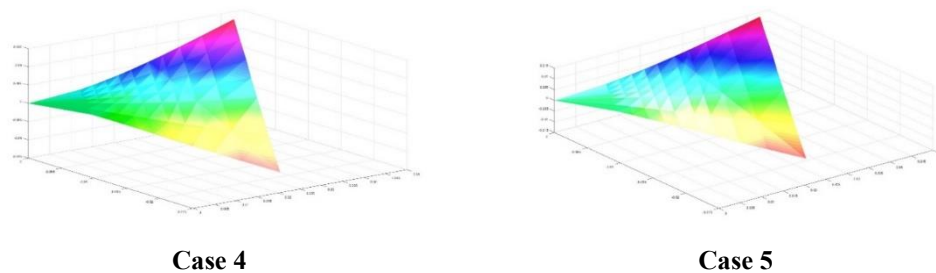


Fig 3.9 Mode 2 a) Case 2 ~ 5 b) Color bands denote displacement

Fig 3.9 shows the change of Mode 2, which is the torsion mode, under different vein arrangements. As seen in Mode 1, here the value of nodes displacement in z-direction drops as well with more veins added to the wing structure. It is also because the structure stiffness is strengthened by the added longitudinal veins.

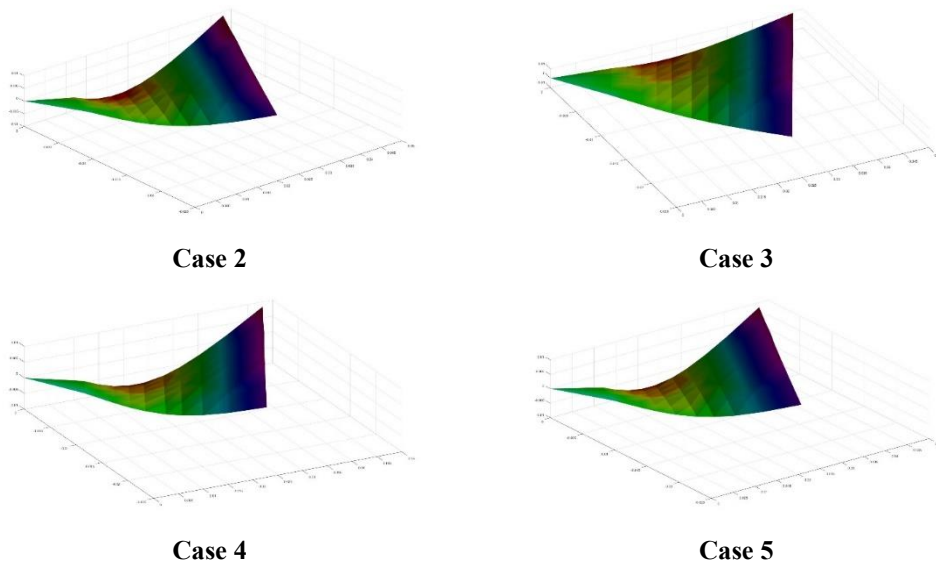


Fig 3.10 Mode 3 a) Case 2 ~ 5 b) Color bands denote displacement

Fig 3.10 shows the change of Mode 3 under different arrangements. Here, the color bands denote the displacement of each node. As shown in the figure, the red area near the proximal area shrinks along with the increase number of veins, which indicates the decrease of displacement values of the related nodes due to the strengthened stiffness. In other words, the torsion has been weakened by the stiffened structure.

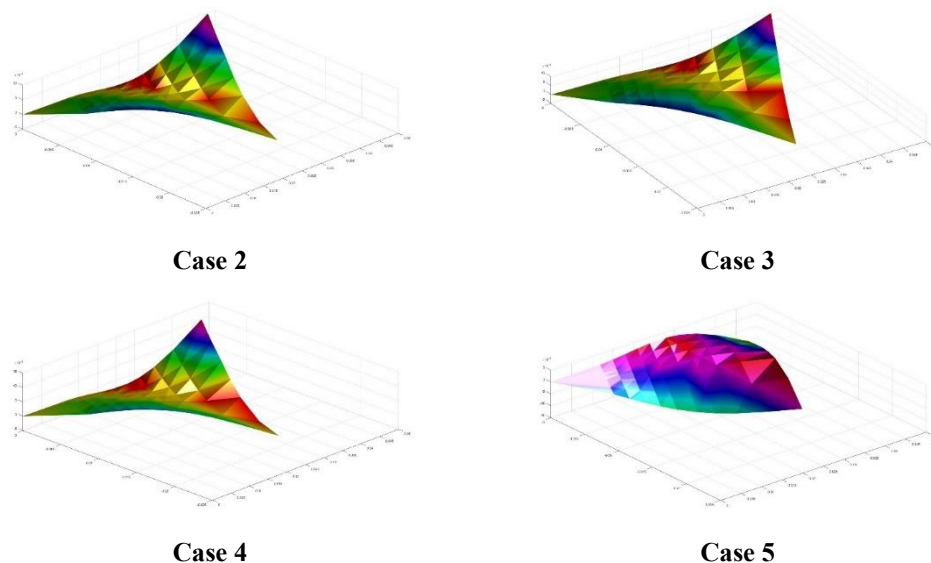
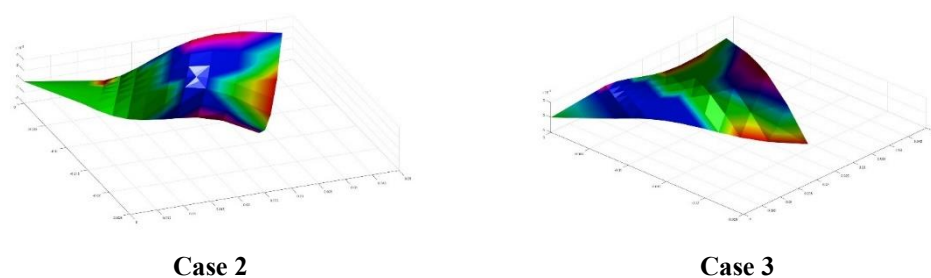


Fig 3.11 Mode 4 a) Case 2 ~ 5 b) Color bands denote displacement

Fig 3.11 shows the change of Mode 4 under different vein arrangements. Unlike the previous cases, the node displacement does not always decrease along with the increasing number of veins. When the vein is added to the leading edge in Case 2, rather than decreasing, the displacement increase at most of the nodes on the wing structure. However, in Case 3, the node displacement decrease when the vein is added to the central line. The displacement keeps decreasing while more veins are added to both sides of the central line. Given the observed facts, it can be assumed that the reason why the displacement in Case 2 increases is that adding longitudinal vein to the leading edge disturbs the structure balance, which eventually leads to the exacerbation of torsion in Case 2. The balance is soon restored by adding more veins near the central line, thus the node displacement decreases again.



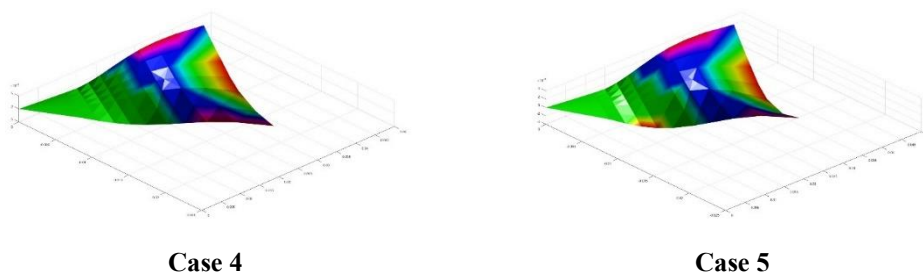


Fig 3.12 Mode 5 a) Case 2 ~ 5 b) Color Denotes the Displacement

Fig 3.12 shows the change of Mode 5 from Case 2 to Case 5. The node displacement in most part of the wing structure decreases while more veins are added, especially in the proximal part close to the supporting point. As seen in the figure, the red area which denotes the deflection in the proximal part totally disappears in the Case 4. On the contrary, the displacement of where denoted by the green band and the nodes near the wing tips increases while the veins are added.

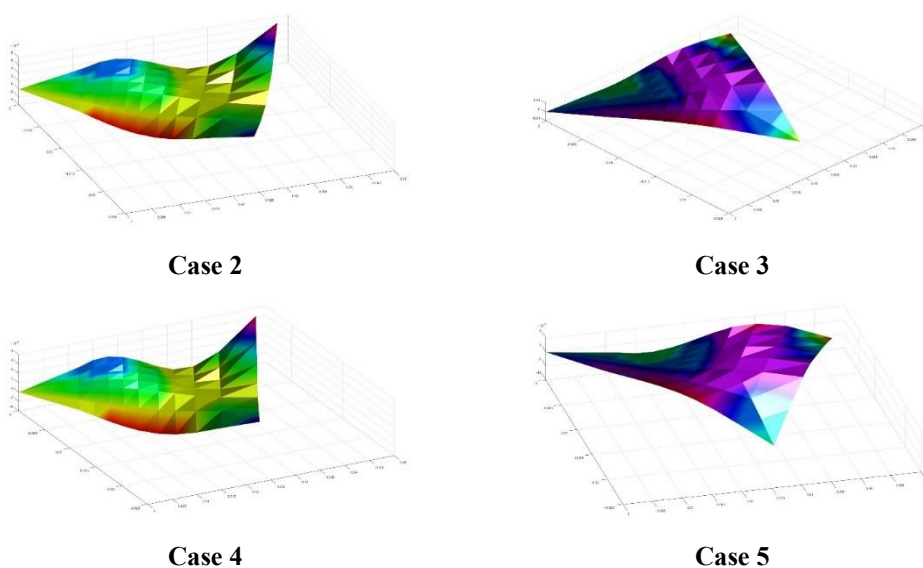


Fig 3.13 Mode 6 a) Case 2 ~ 5 b) Color Denotes the Displacement

Fig 3.13 shows the change of Mode 6 from Case 2 to Case 5. It can be noticed that, in contrast to what observed in Mode 5, the node displacement in most part of the wing structure increases. However, just like the previous case, the displacement near the side edge decreases along with the increasing number of veins.

3.3.3 Effects of the Cross Veins Arrangements

3.3.3.1 Effects on the Natural Frequencies

	Case1	Case6	Case7	Case8	Case9	Case10
Mode1	3.17E+00	3.55E+00	3.56E+00	3.60E+00	3.62E+00	3.62E+00
Mode2	1.47E+01	1.55E+01	1.57E+01	1.61E+01	1.64E+01	1.65E+01
Mode3	3.99E+01	4.25E+01	4.29E+01	4.33E+01	4.37E+01	4.39E+01
Mode4	8.70E+01	8.99E+01	9.17E+01	9.20E+01	9.22E+01	9.51E+01
Mode5	1.42E+02	1.48E+02	1.50E+02	1.51E+02	1.51E+02	1.54E+02
Mode6	1.67E+02	1.76E+02	1.77E+02	1.79E+02	1.81E+02	1.83E+02

Table 3.6 Natural Frequencies of Case1 & Case 6 to 10

	Case1	Case6	Case7	Case8	Case9	Case10
Mode1	100%	111.79%	112.07%	113.33%	113.93%	113.96%
Mode2	100%	105.43%	106.79%	109.50%	111.61%	112.15%
Mode3	100%	106.70%	107.58%	108.63%	109.53%	110.14%
Mode4	100%	103.34%	105.38%	105.74%	106.02%	109.31%
Mode5	100%	104.08%	105.00%	105.84%	106.19%	108.51%
Mode6	100%	105.21%	106.23%	107.37%	108.08%	109.82%

Table 3.7 Increment Percentages of Natural Frequencies

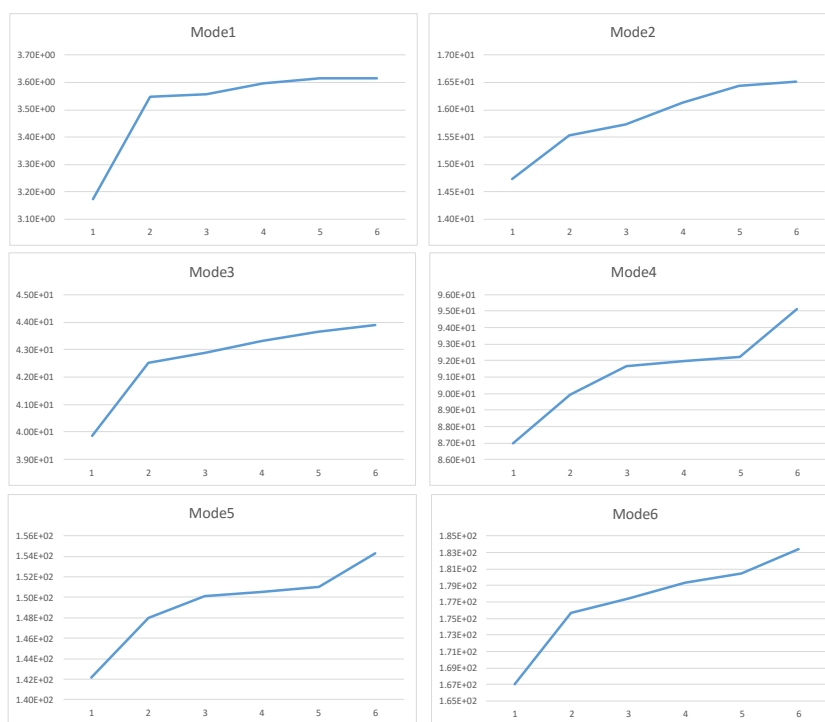


Fig 3.14 The change of corresponding natural frequencies for each mode

The effects on the natural frequencies due to different arrangements of the cross veins are shown in the Table 3.6, Table 3.7 and Fig 3.14. For Mode 1, the average percentage increment of natural frequency is less than one percent, which is almost negligible. The effect on the natural frequency of Mode 2, which is the torsion mode, is greater than Mode 1, but it is still relatively smaller than what is observed in the last section. For Mode 3, the effect is not so obvious as well. Generally, the effect on the frequency of Mode 4, Mode 5 and Mode 6 is also quite inconsiderable. Nonetheless, it is still notable that adding cross veins to the remote part that is near the side edge has a much greater influence to the natural frequency than adding veins to the proximal area of the wing structure.

3.3.3.2 Effects on the Modeshapes

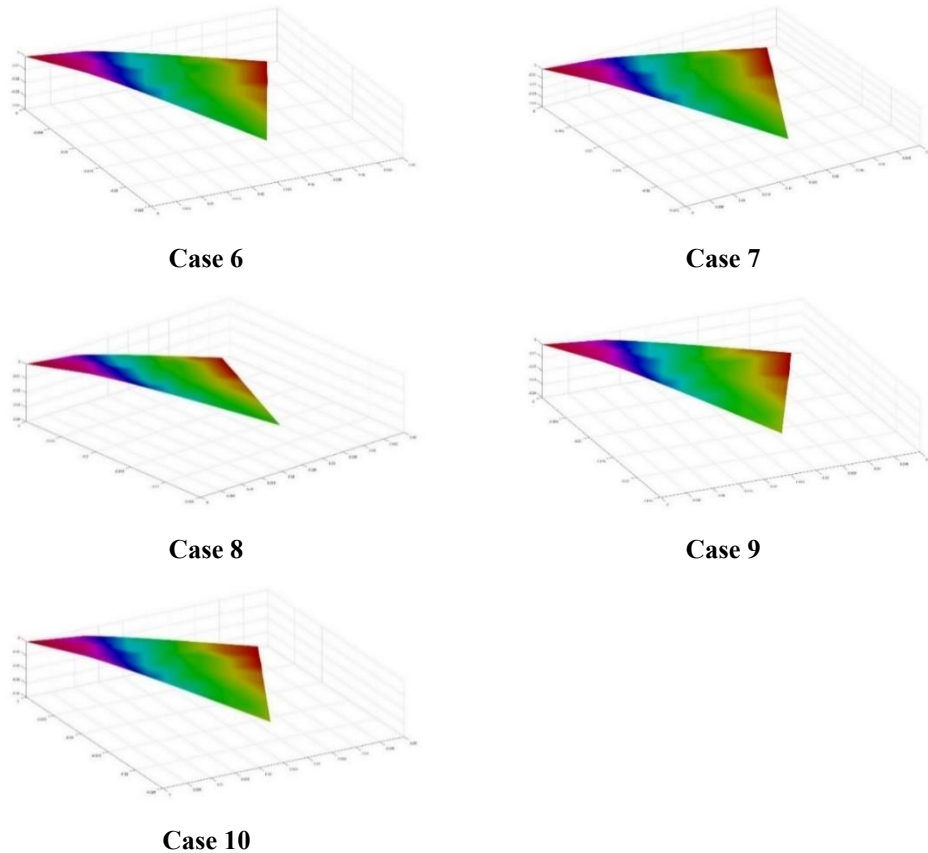


Fig 3.15 Mode 1 a) Case 6 ~ 10 b) Color bands denote displacement

Fig 3.15 shows the change of Mode 1 from Case 6 to Case 10. In general, the node displacement all over the wing structure increases due to the cross veins added to it. However, the average value of increase is really small, which is only around 1% of the original value. The rotations about X-axis and Y-axis also change slightly by the arrangements and do not have any considerable impact on the structure performance. Considering the outcome regarding the natural frequency in the previous context, we can now assert that the cross vein arrangements is not a key factor to the change of Mode 1 because of its limited effect to the structure performance in this Mode.

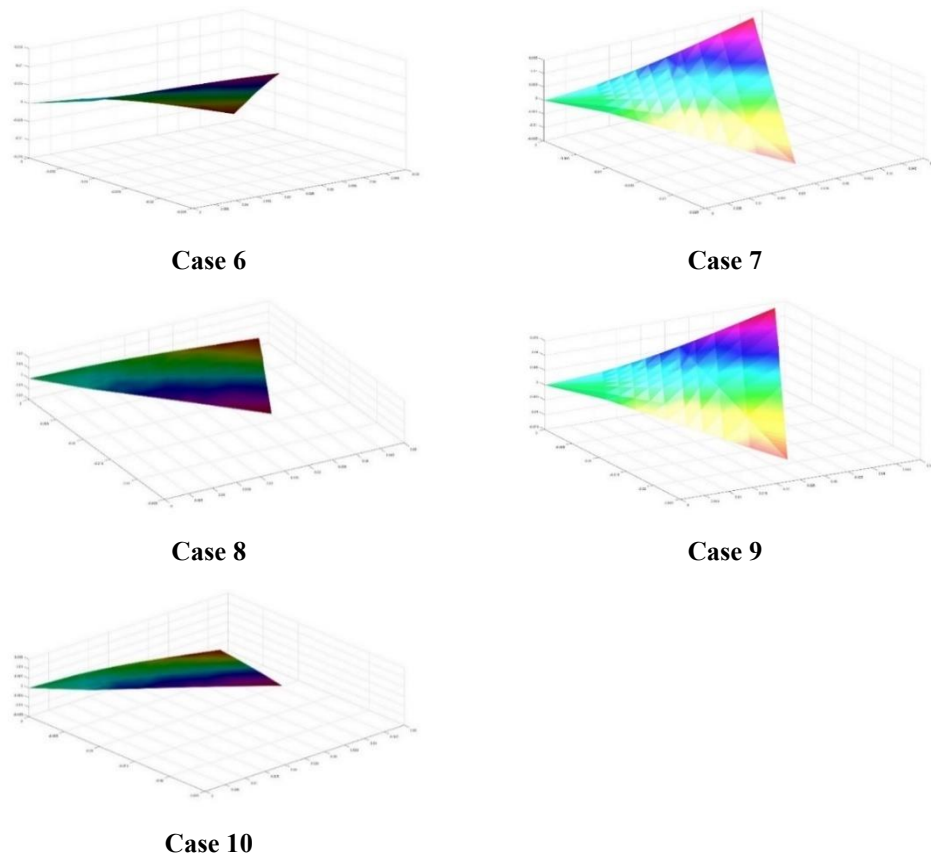


Fig 3.16 Mode 2 a) Case 6 ~ 10 b) Color bands denote displacement

Fig 3.16 shows the performance of Mode 2 under different cross veins arrangements. Adding cross veins to different part of the structure has different effects on Mode 2, the Torsion Mode. According to the results of the test, we can find that adding veins to the proximal area that is near to the supporting

point will cause the decrease of node displacement in the whole wing area. On the other hand, the displacement will increase when cross veins are added to the remote part, which is near to the side edge.

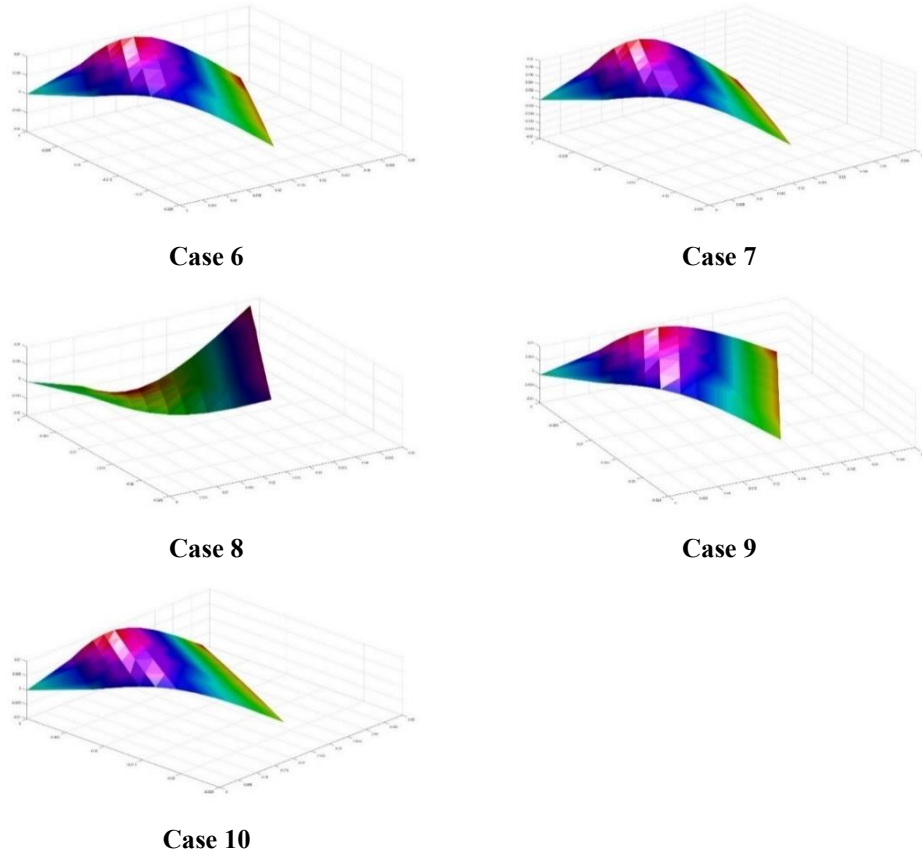


Fig 3.17 Mode 3 a) Case 6 ~ 10 b) Color bands denote displacement

Fig 3.17 shows the Mode 3 in the five different cases. When the first cross vein added to the structure in Case 6, the node displacement in the whole area decrease. Then we add one cross vein to each side of the vein added in the last Case, surprisingly, the displacement is increased even the structure is actually stiffened by the two added veins. To further explore the effect of the cross veins, more cross veins are added to the proximal part of the wing in the following Case 8 and Case 9. After analyzing the results, we can find that the displacement near the supporting point decreases in both of the cases, which implies that the torsion and bending motion in this area can be resisted by the added veins. Nevertheless, only random changes in a relatively small scale can be observed after adding the two veins. In the Case 10,

another two veins are added to the remote part, which lead to a considerable increase of displacement to the whole structure. Then we can have the conclusion that adding cross veins to the proximal area can resist the deformation around the veins yet not much difference will be made to the remote part. At the same time, adding cross veins to the remote part will enhance the deformation in the whole structure.

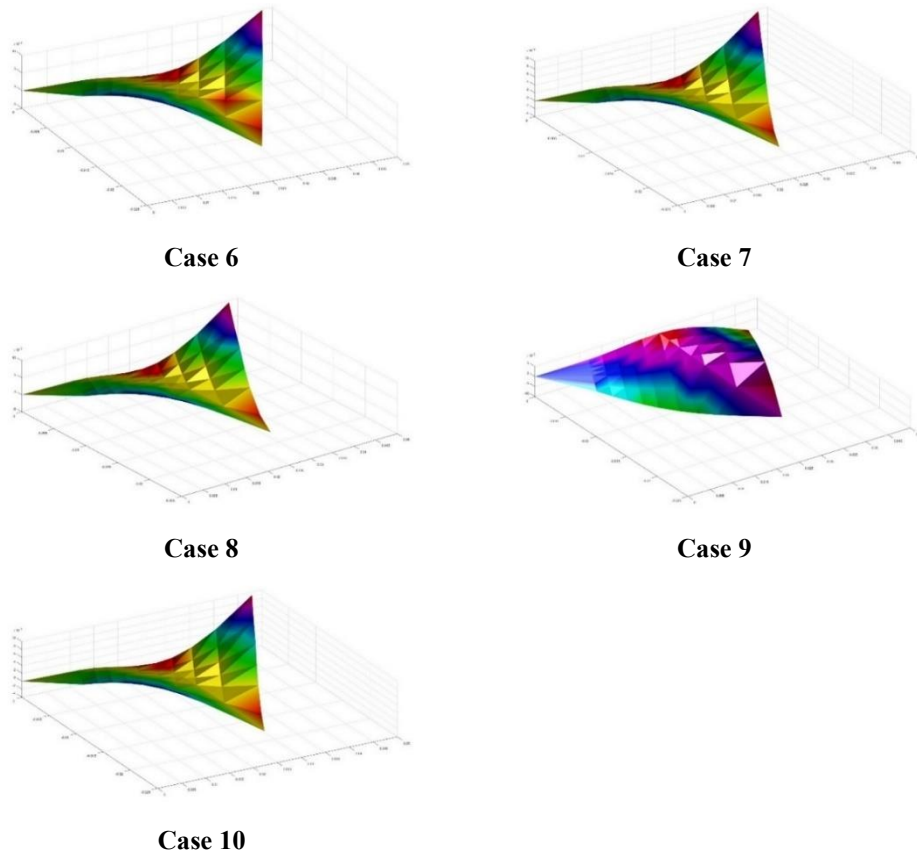


Fig 3.18 Mode 4 a) Case 6 ~ 10 b) Color bands denote displacement

Mode 4 from Case 6 to Case 10 is shown in the Fig 3.18. In general, the displacement is decreased by the added cross veins, despite a small part of it is increased. The most obvious example can be observed in the Case 10, where most of the red band which can be seen in the previous Cases is eliminated. Based on the result of the analysis, it can be suggested that the torsion happens in the remote part can be resisted by the added cross veins, regardless of their positions.

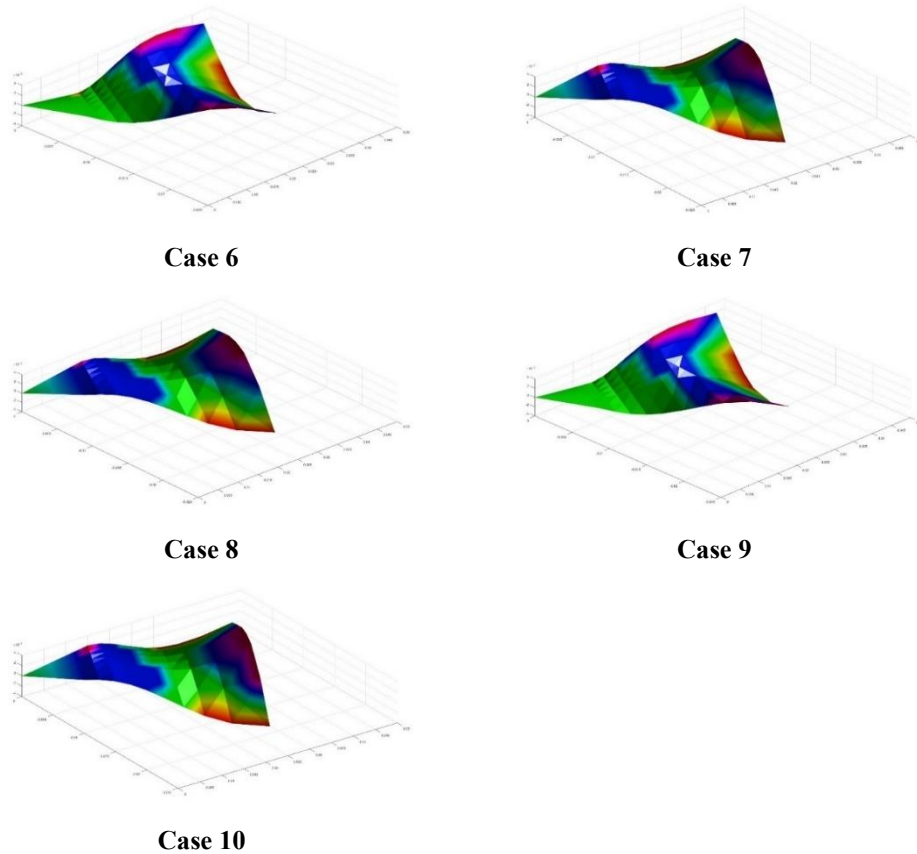


Fig 3.19 Mode 5 a) Case 6 ~ 10 b) Color bands denote displacement

The Fig 3.19 represents the change of Mode 5, the saddle mode, in the five cases. The effects of the cross veins on the structure performance can be concluded as the following: 1) Adding cross veins to the proximal area will lead to the increase of displacement in the most of the wing area while the displacement in certain part may decrease. 2) Adding cross veins to the remote area will cause the increase of displacement over the whole area, except for a small part of it will remain decreasing. 3) In most cases, the cross veins added to the remote area will have more significant influence than the veins added near the supporting point.

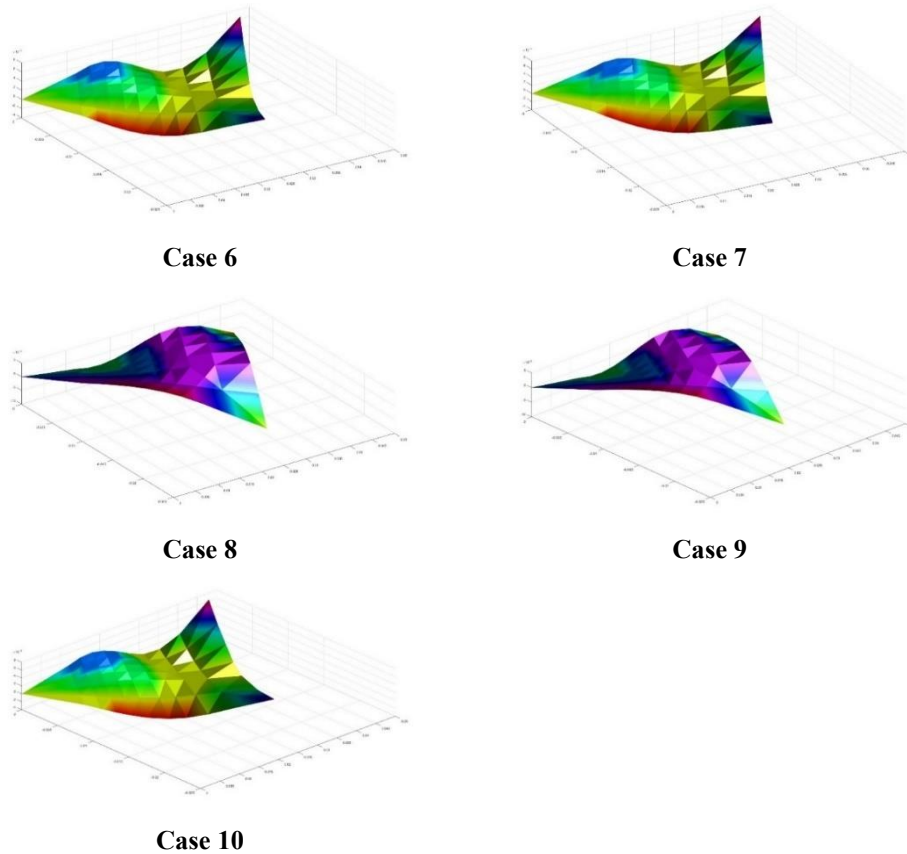


Fig 3.20 Mode 6 a) Case 6 ~ 10 b) Color bands denote displacement

The Fig 3.20 shows the change of Mode 6 from Case 6 to Case 10. In this case, the effect of the added cross veins is more likely to enhance the deformation of the structure under the natural frequency. In Case 10, we can see that the increase of node displacement usually happens near the added veins and the wing edge. However, under certain circumstances, the node displacement may also be decreased. As seen in Case 7, adding veins to both sides of the middle line leads to the tendency of displacement decrease in most part of the wing. In Case 8, even though the node displacement in the proximal area is increased, the displacement in the remote part is still decreased. By adding more veins to the proximal area, even the displacement in such area is eventually decreased. Till now, we may conclude that the either adding cross veins to the proximal or the remote area will lead to the increase of node displacement. Yet, by adding cross veins carefully to the proximal area and control the number of veins we use, it is still possible to resist the structure deformation in Mode 6.

3.3.4 Effects of the Combined Vein Arrangements

3.3.4.1 Effects on the Natural Frequencies

	Case1	Case11	Case12	Case13
Mode1	3.17E+00	4.96E+00	4.98E+00	5.04E+00
Mode2	1.47E+01	1.86E+01	1.89E+01	1.96E+01
Mode3	3.99E+01	5.05E+01	5.09E+01	5.21E+01
Mode4	8.70E+01	9.95E+01	1.01E+02	1.05E+02
Mode5	1.42E+02	1.61E+02	1.64E+02	1.69E+02
Mode6	1.67E+02	1.92E+02	1.94E+02	2.01E+02

Table 3.8 Natural Frequencies of Case1 & Case 11 to 13

	Case1	Case11	Case12	Case13
Mode1	100%	156.45%	156.92%	158.97%
Mode2	100%	126.48%	127.97%	132.86%
Mode3	100%	126.67%	127.65%	130.66%
Mode4	100%	114.31%	116.32%	120.46%
Mode5	100%	113.50%	115.19%	118.57%
Mode6	100%	115.15%	116.41%	120.24%

Table 3.9 Increment Percentages of Natural Frequencies



Fig 3.21 The change of corresponding natural frequencies for each mode

Case 11 to Case 13 are tested and the obtained natural frequencies are shown in the Table 3.8. Table 3.9 shows increment of natural frequency compared to Case 1. Fig 3.21 shows the change of corresponding natural frequencies for each mode. By analyzing the tests results, we can see that the frequency increment due to the combined veins arrangements is very close the sum of the increment due to longitudinal veins and cross veins, of which the errors are less than 1%.

By comparing the contribute of cross veins and longitudinal veins to the frequency increment, we can find that the influence of the later one is much more considerable than the former. The ratio of the contribute due to cross veins to the contribute due to longitudinal veins ranges from 0.06 to 0.4. The smallest one can be seen in Case 1 while the highest value can be found in Case 4. For Case 2 and Case 3, the ratio is 0.28 and 0.156, respectively. For Case 5 and Case 6, the ratio is around 0.4.

Based on the analysis above, we can suggest that the longitudinal veins always play a major part in the change of natural frequency. The effect of cross veins is more apparent on the relatively high frequencies than on the lower ones.

3.3.4.2 Effects on the Modeshapes

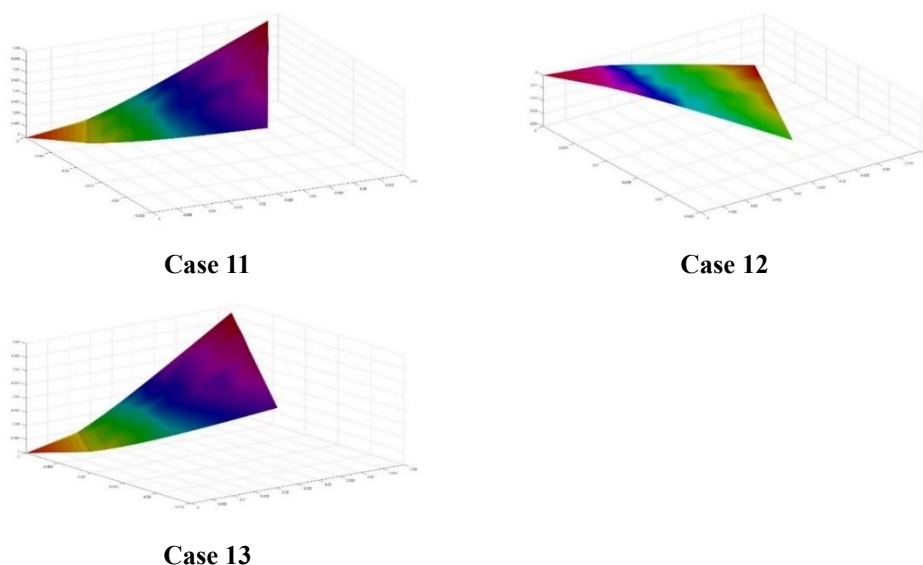


Fig 3.22 Mode 1 a) Case 11 ~ 13 b) Color bands denote displacement

Fig 3.21 shows the change of Mode 1 from Case 11 to Case 13. By comparing Case 11 with Case 6, similar effect of longitudinal veins, which has been discussed in the section 3.2.2.2, can be observed. So does comparing Case 7 with Case 12 and comparing Case 5 with Case 13.

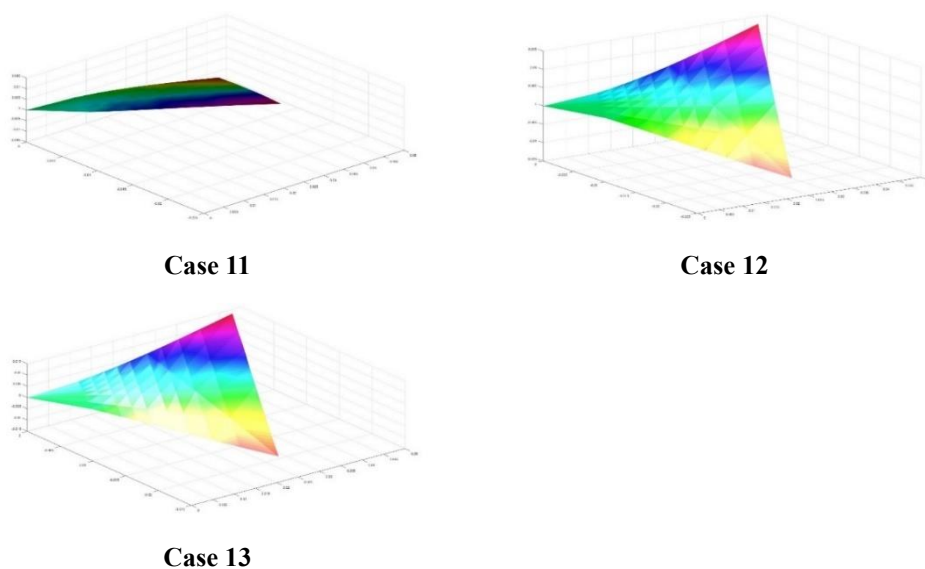
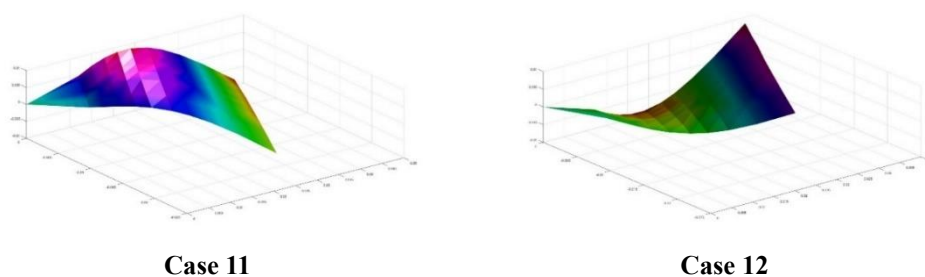
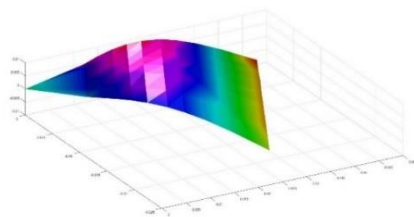


Fig 3.23 Mode 2 a) Case 11 ~ 13 b) Color bands denote displacement

Fig 3.23 shows the change of Mode 2 from Case 11 to Case 13. After analyzing the effect of adding two different kinds of vein to the structure, it can be noticed that adding longitudinal veins is more effective at reducing the node displacement in the proximal area than adding cross veins. On the other hand, it is also confirmed that, in a mixed situation, adding cross veins can still enhance the deformation in the remote area.

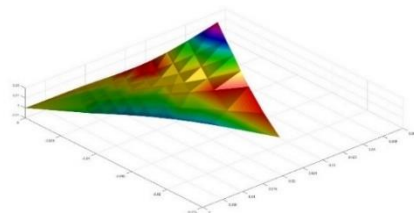




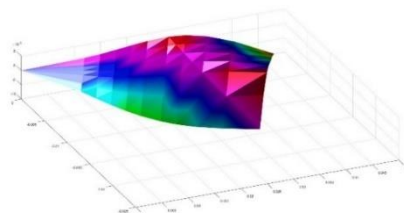
Case 13

Fig 3.24 Mode 3 a) Case 11 ~ 13 b) Color bands denote displacement

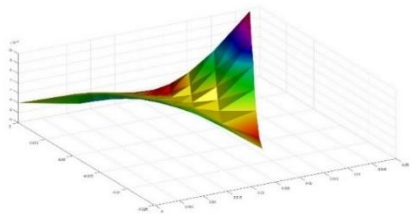
In Fig 3.24, the change of Mode 3 from Case 11 to Case 13 is shown. Given the comparison between Case 11 and Case 6, node displacement in the whole area is decreased with the added longitudinal veins. The same conclusion can be found by comparing Case 5 and Case 11. Moreover, it should be pointed out that the value of placement decrease in the remote area is smaller than the value in the proximal area. By comparing Case 5, Case 10 and Case 13, it can be seen that the displacement increase due to longitudinal veins is smaller than the increase due to cross veins. Meanwhile, the displacement decrease due to longitudinal veins is larger than the decrease due to cross veins. Thus, we can suggest that adding longitudinal veins can enhance the displacement decrease in the wing structure with cross veins. It can also weaken the displacement increase due to the cross veins. Since the value of displacement decrease is usually larger than the value of displacement increase due to the cross veins, the tendency of displacement increase caused by the cross veins can be inverted by adding longitudinal veins.



Case 11



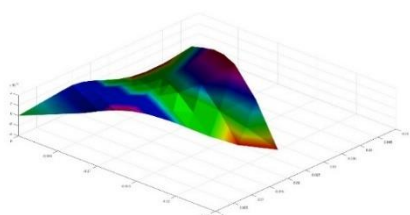
Case 12



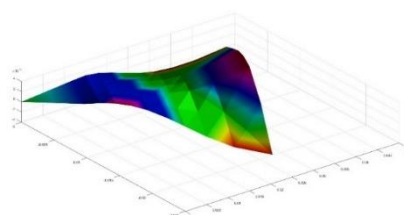
Case 13

Fig 3.25 Mode 4 a) Case 11 ~ 13 b) Color bands denote displacement

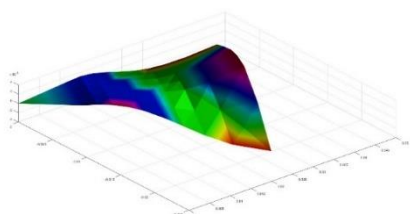
The change of Mode 4 is shown in Fig 3.25. As seen in the previous sections, the overall tendency of the change of node displacement is decreasing. However, the value of displacement decrease here is not always among the two values obtained in the uncombined arrangement cases. Sometimes it's even higher than either of them, which shows that the results of the combined arrangements here are not simply sum of the results of two independent cases, but include interaction between longitudinal and cross veins.



Case 11



Case 12



Case 13

Fig 3.26 Mode 5 a) Case 11 ~ 13 b) Color bands denote displacement

Fig 3.26 shows the change of Mode 5 from Case 11 to Case 13. For the saddle mode, the effect of either adding cross veins or adding longitudinal veins still follows the principle discussed in the two previous sections. And the value of displacement change is among the values obtained in component

cases. In the meantime, the value of displacement decrease in certain area is still higher than both of the values we have in the component cases, which means the interaction seen in the last section still exists.

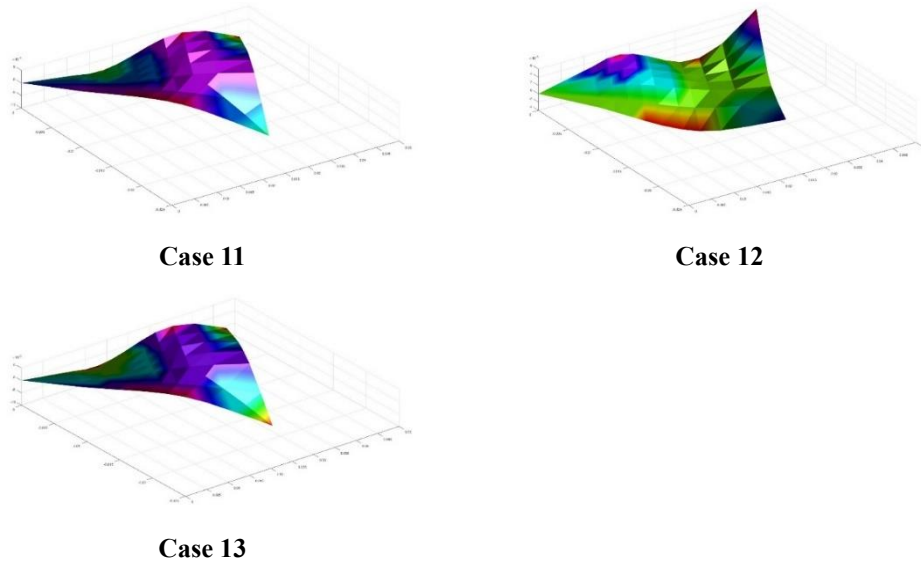


Fig 3.27 Mode 6 a) Case 11 ~ 13 b) Color bands denote displacement

Fig 3.27 shows the change of Mode 6 from Case 11 to Case 1. When adding cross veins and adding longitudinal veins both lead to increase of displacement at the nodes, the increment value at most of the nodes tends to be higher than the values seen in each of the component cases. Otherwise, the value of displacement change will most likely to be among the values obtained in each case that form the combined arrangement. Only at a few nodes that the displacement decrease due to the combined arrangements is higher than both of the component cases.

Chapter Four

Conclusions and Future Work

4.1 Conclusions

After conducting all the thirteen test cases and analyzing the effects of different vein arrangements on the six dominant modes and corresponding eigenvalues of each case, the effects of longitudinal veins and cross veins to each mode are concluded, respectively.

From the research, we can see that both the longitudinal veins and the cross veins can change the natural frequencies of the structure. However, the longitudinal vein plays a much more considerable role in the change of natural frequency when compared with the cross veins. In other words, the stiffness of the structure is mainly influenced by the longitudinal veins.

The effects of adding veins on the insect wing deformation sometimes varies within structure, rather than yield the general tendency in the whole area. Adding veins to the different area in the same structure will cause different consequences. In certain cases, it even reverses the deformation.

When the arrangement consists of both longitudinal veins and cross veins, the change of deformation will be compromised in most cases. Nonetheless, the change will occasionally be dominated by one of them if the change of deformation is inverse to each other and the values of change differ greatly.

Moreover, it is also observed that, in some cases, the deformation change is strengthened and the value of change is even higher than any of the original values obtained in the component cases, which indicates a possible relationship between the cross veins and longitudinal veins in the combined arrangements.

4.2 Future Work

The analysis of the natural frequencies and the corresponding modeshapes is only the first step of structural dynamic analysis. It gives us a general picture of how the vein arrangements change the deformation of wing structure under varies natural frequencies and it is conducted in the semi-static situation without any applied load.

In future work, the interaction between the wing structure and the airflow should be considered in the test process. Additionally, the Newmark method will be introduced in order to analyze the deformation of insect wings in the flapping motion. A more refined Finite Element Modelling of the wing structure will also be developed in future tests, along with more carefully planned test cases. In future, not only the general deformation changes will be discussed, the detailed principles behind the changes will be analyzed as well, especially the potential relationships between these two kinds of veins.

All the work mentioned above is to serve the ultimate goal of the research, that is, to design a much more efficient wing structure with optimized vein distribution for the future insect-like Micro Air Vehicles.

Reference

- [1] Sims, T. W., Palazotto, A. N., & Norris, A. (2010). A structural dynamic analysis of a *Manduca sexta* forewing. *International Journal of Micro Air Vehicles*, 2(3), 119-140.
- [2] O'Hara, R. P. (2012). *The Characterization of Material Properties and Structural Dynamics of the Manduca Sexta Forewing for Application to Flapping Wing Micro Air Vehicle Design*.
- [3] Combes, S. A., & Daniel, T. L. (2003). Flexural stiffness in insect wings I. Scaling and the influence of wing venation. *Journal of experimental biology*, 206(17), 2979-2987.
- [4] Dirks, J. H., & Taylor, D. (2012). Veins improve fracture toughness of insect wings. *PloS one*, 7(8), e43411.
- [5] Wootton, R. (2002). Insect wings: the world's smallest, smartest aerofoils. *Biologist (London, England)*, 49(3), 97-100.
- [6] Wootton, R. J., Herbert, R. C., Young, P. G., & Evans, K. E. (2003). Approaches to the structural modelling of insect wings. *Philosophical Transactions of the Royal Society of London B: Biological Sciences*, 358(1437), 1577-1587.
- [7] Wootton, R. J. (1992). Functional morphology of insect wings. *Annual review of entomology*, 37(1), 113-140.
- [8] Barras, F. (2011). 3-D Bernoulli Beams within Akantu. *Semester Project, LSMS-EPFL*.
- [9] Allman, D. J. (1988). Evaluation of the constant strain triangle with drilling rotations. *International Journal for Numerical Methods in Engineering*, 26(12), 2645-2655.
- [10] Allman, D. J. (1996). Implementation of a flat facet shell finite element for applications in structural dynamics. *Computers & structures*, 59(4), 657-663.
- [11] Reddy, J. N. (1993). *An introduction to the finite element method* (Vol. 2, No. 2.2). New York: McGraw-Hill.

Appendices

A1. Triangular Coordinates:

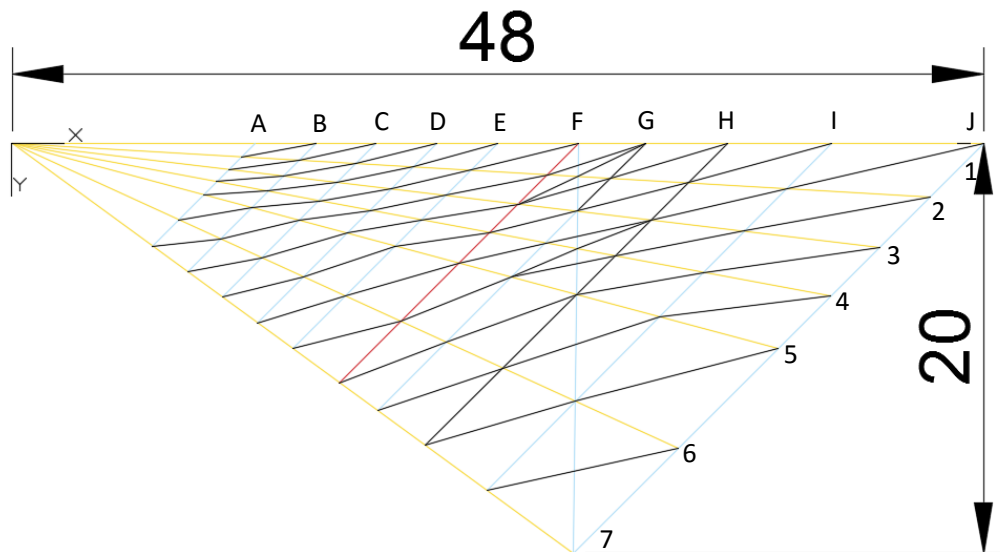
$$L_i = \frac{1}{2A}(A_i^0 + a_i x + b_i y)$$

$$\begin{cases} A_i^0 = x_j y_l - x_l y_j \\ a_i = y_j - y_l = y_{jl} \\ b_i = x_l - x_j = x_{lj} \end{cases}$$

$$\begin{cases} \frac{\partial L_i}{\partial x} = \frac{a_i}{2A} \\ \frac{\partial L_i}{\partial y} = \frac{b_i}{2A} \end{cases}$$

$$\begin{cases} c_{ij} = \cos \gamma_{ij} = \frac{-a_l}{l_{ij}} \\ s_{ij} = \sin \gamma_{ij} = \frac{-b_l}{l_{ij}} \end{cases}$$

A.2 Node Coordinate:



	A	B	C	D	E	F	G	H	I	J
1	[12,0,0]	[15,0,0]	[18,0,0];	[21,0,0]	[24,0,0]	[28,0,0]	[31.30,0,0]	[35.37,0,0]	[40.50,0,0]	[48,0,0]
2	[11.3446,- 0.6546,0]	[14.1808,- 0.8182,0]	[17.0169,- 0.9819,0]	[19.8531,- 1.1455,0]	[22.6892,- 1.3092,0]	[26.4707,- 1.5274,0]	[27.9864,- 1.0479,0]	[33.4367,- 1.9293,0]	[38.2993,- 2.2099,0]	[45.38,- 2.62,0]
3	[10.7188,- 1.2797,0]	[13.3984,- 1.5996,0]	[16.0781,- 1.9195,0]	[18.7578,- 2.2394,0]	[21.4375,- 2.5593,0]	[25.0104,- 2.9859,0]	[27.9790,- 1.6144,0]	[31.5921,- 3.7717,0]	[36.1990,- 4.3217,0]	[42.98,- 5.12,0]
4	[10.1153,- 1.8824,0]	[12.6441,- 2.3530,0]	[15.1730,- 2.8236,0]	[17.7018,- 3.2942,0]	[20.2306,- 3.7648,0]	[23.6024,- 4.3922,0]	[29.5889,- 1.7073,0]	[27.9405,- 4.5693,0]	[34.1726,- 6.3593,0]	[40.46,- 7.53,0]
5	[9.4671,- 2.5298,0]	[11.8338,- 3.1623,0]	[14.2006,- 3.7947,0]	[16.5674,- 4.4272,0]	[18.9341,- 5.0596,0]	[22.0898,- 5.9029,0]	[27.9719,- 2.1589,0]	[27.9323,- 5.1980,0]	[31.9942,- 8.5496,0]	[37.87,- 10.1,0]

6	[8.2305,- 3.7649,0]	[10.2881,- 4.7061,0]	[12.3457,- 5.6474,0]	[14.4033,- 6.5886,0]	[16.4609,- 7.5298,0]	[19.2044,- 8.7848,0]	[27.9719,- 3.3223,0]	[29.8135,- 5.5481,0]	[27.8343,- 12.7324,0]	[32.9,- 15.1,0]
7	[6.9341,- 5.0596,0]	[8.6677,- 6.3246,0]	[10.4012,- 7.5895,0]	[12.1347,- 8.8544,0]	[13.8683,- 10.1193,0]	[16.1797,- 11.8058,0]	[26.3826,- 4.9096,0]	[27.9227,- 5.9358,0]	[23.4673,- 17.1234,0]	[27.74,- 20.2,0]
8							[24.6919,- 6.5983,0]	[27.9029,- 7.4563,0]	[27.8710,- 9.9071,0]	
							[21.4666,- 9.8196,0]	[24.2582,- 11.0966,0]		
							[18.0856,- 13.1965,0]	[20.4375,- 14.9126,0]		

A.3 The top view and side view of the modeshape

